REPORT DOCUMENTATION PAGE	Form Approved OMB No. 0704-0188

The public reporting burden for this collection of information is estimated to average 1 hour per response, including the time for reviewing instructions, searching existing data sources, gathering and maintaining the data needed, and completing and reviewing the collection of information. Send comments regarding this burden estimate or any other aspect of this collection of information, including suggestions for reducing the burden, to the Department of Defense, Executive Service Directorate (0704-0188). Respondents should be aware that notwithstanding any other provision of law, no person shall be subject to any penalty for failing to comply with a collection of information if it does not display a currently valid OMB control number.
PLEASE DO NOT RETURN YOUR FORM TO THE ABOVE ORGANIZATION.

1. REPORT DATE (DD-MM-YYYY)	2. REPORT TYPE	3. DATES COVERED (From - To)
02/10/2008	Final Report	July 2006-June 2008

4. TITLE AND SUBTITLE
NACE Seed Grant Program. Final Report from Seed Grant Recipient Todd Allen, "Microstructural Effects on the Corrosion Behavior of Alloys and Ceramics"

5a. CONTRACT NUMBER

5b. GRANT NUMBER
N00014-02-1-0024

5c. PROGRAM ELEMENT NUMBER

6. AUTHOR(S)
Allen, Todd; Tan, Lizhen

5d. PROJECT NUMBER

5e. TASK NUMBER

5f. WORK UNIT NUMBER

7. PERFORMING ORGANIZATION NAME(S) AND ADDRESS(ES)
NACE International
1440 South Creek Dr.
Houston, TX 77084-4906

8. PERFORMING ORGANIZATION REPORT NUMBER

9. SPONSORING/MONITORING AGENCY NAME(S) AND ADDRESS(ES)
Office of Naval Research
875 Randolph Street
Arlington, VA 22203-1995

10. SPONSOR/MONITOR'S ACRONYM(S)
ONR

11. SPONSOR/MONITOR'S REPORT NUMBER(S)

12. DISTRIBUTION/AVAILABILITY STATEMENT
FINAL REPORT APPROVED FOR PUBLIC RELEASE. Allen's papers are listed on p. 36 of the report.

13. SUPPLEMENTARY NOTES

20081014060

14. ABSTRACT
The objective of this research was to investigate the effect of microstructure on the corrosion behavior of metals and ceramics. Representative materials from the important engineering alloys and ceramics were studied to determine their corrosion behavior in supercritical water and during cyclic oxidation in air. The materials included Incoloy alloy 800H, Inconel alloy 617, 12%Cr ferritic-martensitic steel HCM12A, and silicon carbide fabricated by means of chemical vapor deposition (CVD). The study focused on the effect of the microstructure such as grain boundary networks, grain size, and residual strains on the corrosion behavior of these materials. Novel grain boundary engineering and commercial shot-peening were employed to adjust the grain boundary character distribution of the metals and refine the surface grain size of alloy 800H, respectively. The effect of residual strains generated from the CVD processing was studied for SiC.

15. SUBJECT TERMS
grain boundary, scanning electron microscopy, transmission electron microscopy, residual strains, corrosion, oxidation, supercritical water, shot peening, X-ray photoelectron spectroscopy, X-ray diffraction/grazing incidence X-ray diffraction, inverse pole figure, energy dispersive X-ray spectroscopy, chemical vapor deposition

16. SECURITY CLASSIFICATION OF:			17. LIMITATION OF ABSTRACT	18. NUMBER OF PAGES	19a. NAME OF RESPONSIBLE PERSON
a. REPORT	b. ABSTRACT	c. THIS PAGE			Linda Goldberg
U	U	U	UU	44	19b. TELEPHONE NUMBER (Include area code) 281-228-6221

Standard Form 298 (Rev. 8/98)
Prescribed by ANSI Std. Z39.18
Adobe Professional 7.0

Project Title: Microstructural Effects on the Corrosion Behavior of Alloys and Ceramics

Covering Period: June 2006 through June 2008

Date of Report: June 30, 2008

Recipient: University of Wisconsin-Madison
                        1500 Engineering Dr
                        Madison, WI 53705

Principal Investigator: Todd Allen, 608-265-4083, allen@engr.wisc.edu
Other Investigators: Lizhen Tan

Project Objective

The objective of this research was to investigate the effect of microstructure on the corrosion behavior of metals and ceramics. Representative materials from the important engineering alloys and ceramics were studied to determine their corrosion behavior in supercritical water and during cyclic oxidation in air. The materials included Incoloy alloy 800H, Inconel alloy 617, 12%Cr ferritic-martensitic steel HCM12A, and silicon carbide fabricated by means of chemical vapor deposition (CVD). The study focused on the effect of the microstructure such as grain boundary networks, grain size, and residual strains on the corrosion behavior of these materials. Novel grain boundary engineering and commercial shot-peening were employed to adjust the grain boundary character distribution of the metals and refine the surface grain size of alloy 800H, respectively. The effect of residual strains generated from the CVD processing was studied for SiC.

Abbreviations

AR	As-Received
CSL	Coincidence Site Lattice
CSLBs	Coincidence Site Lattice Boundaries
CVD	Chemical Vapor Deposition
EBSD	Electron Back-Scatter Diffraction
EDS	Energy Dispersive x-ray Spectroscopy
GBCD	Grain Boundary Character Distribution
GBE	Grain Boundary Engineering
GBs	Grain Boundaries
HABs	High Angle Boundaries
IPF	Inverse Pole Figure
LABs	Low Angle Boundaries
SCW	Super-Critical Water
SEM	Scanning Electron Microscopy
SP	Shot-Peening
TEM	Transmission Electron Microscopy
TMP	Thermo-Mechanical Processing
XPS	X-ray Photoelectron Spectroscopy
XRD/GIXRD	X-Ray Diffraction/Grazing Incidence X-Ray Diffraction

Table of Contents

1. Background

The corrosion resistance of a material is highly dependent upon the underlying microstructure. Even for alloys with the same composition, different cold/hot-working histories on can result in changes in the base microstructure, leading to significantly different corrosion behavior. This project studied the effect of microstructures, such as grain boundaries, grain size, and residual strains, on the corrosion behavior of advanced steels (Incoloy alloy 800H and ferritic/martensitic steel HCM12A), a nickel-base alloy (Inconel alloy 617), and silicon carbide (SiC).

1.1. Grain boundaries (GBs) and grain boundary engineering (GBE)

GBs are common defects existing in crystalline materials, and play a major factor in determining the physical, mechanical, electrical, and chemical properties of crystalline materials [1]. As a fast diffusion path compared to bulk or lattice diffusion, grain boundaries (GB) play an important role the atomic transport that determines the modes of corrosion. Based on the misorientation between adjacent grains, GBs can be classified as low-angle boundaries (LABs) and high-angle boundaries (HABs) with a misorientation angle of $15°$ as a usual division. Within the coincidence site lattice (CSL) model, which introduces a parameter Σ describing the reciprocal density of coincident sites at a grain boundary, grain boundaries can be classified as $\Sigma 1$ boundaries, low-Σ CSL boundaries (CSLBs, $3 \leq \Sigma \leq 29$), and general boundaries. $\Sigma 1$ boundaries correspond to LABs with misorientation angle $<15°$ [2]. General boundaries include high-Σ CSLBs ($\Sigma > 29$) and non-CSLBs (or random boundaries). Both low-Σ CSLBs and general boundaries correspond to HABs.

Compared to general boundaries, especially random boundaries, low-Σ CSLBs have many special properties such as low boundary energies, less susceptibility to impurity or solute segregation, and greater resistance to grain boundary sliding and intergranular degradation [2]. Thus, the low-Σ CSLBs are often referred as "special boundaries". Among the low-Σ CSLBs, the contribution of $\Sigma 3$ boundaries to property improvements has been found to be the most significant [3,4]. This is because the energy of $\Sigma 3$ boundaries is extremely low, typically about 1/50 of a random boundary [2]. Intergranular oxidation preferentially takes place at general boundaries while low-Σ CSLBs, particularly $\Sigma 3$, $\Sigma 11$, $\Sigma 19$, and $\Sigma 27$ boundaries, have excellent oxidation resistance [5]. Thus, materials with a high fraction of low-Σ CSLBs are expected to have superior corrosion resistance. To take advantage of the special properties of the low-Σ CSLBs, GBE was proposed as an approach to control the properties of crystalline metals by tuning the grain boundary character distribution (GBCD) to obtain a high fraction of low-Σ CSLBs and interrupt the connectivity of generally boundaries. GBE has been successfully employed to enhance strength [6], weldability [7], resistance to creep, [8] and resistance to stress corrosion cracking [9].

Thermomechanical processing (TMP) is the most popular method used to preform GBE. The effect of GBE (achieved by TMP) on the corrosion behavior of alloys 800H and 617 has been studied in this project.

1.2. Grain size

Considering oxidation performance at high temperatures, a fine-grained microstructure is preferable in the case of high-Cr steels while a coarse grain material is superior in case of a low

1

Cr steel [10]. This is because the population of grain boundaries greatly increases with the decrease of grain size. As a result for steels with a high Cr content such as austenitic stainless steel 316, a greater Cr enrichment in the inner oxide scale and subsequently a quicker formation of a protective layer of Cr-rich oxide can easily form. A beneficial effect of nano-scale grains was observed on oxidation of Austenitic 304 stainless steel, which resulted in Cr-rich oxides rather than Fe-rich oxides due to enhanced Cr diffusion and thus prevented breakaway oxidation in wet air [11]. On the contrary, pronounced internal oxidation along grain boundaries and a higher oxidation rate can occur on steels with a low Cr content such as ferritic steel 2.25Cr-1Mo [10].

There are many routes to produce metals with ultrafine grains. One of the popular routes is several plastic deformation. Shot-peening (SP) is a commercial technique used in a wide variety of industries for surface grain refinement of metal parts. It is a cold-working process in which a metal part is bombarded by tiny beads of steel, cut-wire, glass or ceramic shot. The effect of SP on the corrosion behavior of alloy 800H has been studied in this project.

1.3. Residual strains

Strain has been shown to enhance the dissolution of steels in aqueous sodium chloride and sulfuric acid solutions [12]. The strain sign (tensions versus compression) plays a complex effect on stress corrosion [13]. For example, tension strain results in a lower dissolution rate than compression in a short period of time, e.g. ~50 seconds, but changes to a significantly higher dissolution rate in a long period of time. The effect of residual strains, resulting from chemical vapor deposition (CVD) processing, on corrosion behavior of SiC has been studied in this project.

1.4. Materials

1.4.1. Incoloy alloy 800H

Incoloy alloy 800H (UNS N08810, 45Fe-31Ni-20Cr) is an austenitic alloy with a mean grain size greater than ~70 μm in diameter. It is a solid-solution-strengthened alloy with additional strengthening by precipitation of titanium nitrides and carbides such as MN/MC (rich in Ti) and chromium carbides such as $M_{23}C_6$ (rich in Cr). Titanium nitrides are stable at all temperatures below the melting point of the alloy and are therefore unaffected by heat treatment [14]. The detailed specifications of alloy 800H regarding the physical and mechanical properties can be found in Ref. [14]. Alloy 800H, usually used in an annealed condition, has been broadly utilized in furnace components and equipment, petrochemical furnace cracker tubes, pigtails and headers, and sheathing for electrical heating elements since its introduction to the market in the 1950s. Based on its advantages such as high strength and corrosion-resistance at high temperatures, alloy 800H had been selected as one of the potential candidate alloys for Generation IV nuclear plant designs [15,16].

Because of the high Cr and Ni contents, alloy 800H has excellent resistance to oxidation. The Cr in this alloy promotes the formation of a protective surface oxide, and the Ni enhances the protection, especially during cyclic exposure to high temperatures. Otsuka et al studied the oxidation behavior of alloy 800H exposed in high-temperature steam at 700°C, and found that a uniform duplex thin oxide scale formed on alloy 800H [17]. The outer oxide layer is composed of Fe_3O_4 with some Fe_2O_3 involved, and the inner oxide layer primarily an $(Fe,Cr)_3O_4$ spinel.

2

Internal oxides, probably of Cr_2O_3 or Al_2O_3, were observed dispersing within the metal substrate ahead of the inward-growing inner spinel [17,18].

Limited literature has been reported on the oxidation behavior of alloy 800H exposed in supercritical water (SCW). Preliminary result of SCW-exposed alloy 800H at 500°C and 25 MPa indicates severe oxide exfoliation occurred after ~333 hours exposure [19]. Oxide exfoliation is a detrimental phenomenon, which may cause blockage inside superheater/reheater tubes or severe erosion damage at turbine blades [20]. In a nuclear system, it can also lead to redistribution of radioactive material.

To withstand the high-temperature and pressure environment in modern and future power plant system, the properties of alloy 800H need to be improved for extending its service lifetime and thus maintaining system stability. This study was performed to study the corrosion/oxidation behavior of alloy 800H and develop practical approaches to improve the corrosion resistance and mitigate the oxide exfoliation of alloy 800H. GBE and shot-peening (SP) have been developed for alloy 800H in this study to modify grain boundary networks and surface grain size, respectively. The effect of the microstructural changes (grain boundary network and grain size) on the corrosion behavior of alloy 800H is presented in this report.

1.4.2. Inconel alloy 617

Inconel alloy 617 (UNS N06617, Ni-22Cr-13Co-10Mo), an austenitic solid-solution alloy, has been broadly utilized in gas turbines for combustion cans and ducts as well as industrial furnace components and applications where high-temperature corrosion resistance is generally important. Based on its excellent resistance to oxidation in a wide range of corrosive media and excellent high temperature strength, alloy 617 had been selected as a potential candidate alloy for Generation IV nuclear plant designs [21]. Alloy 617 is normally used in a solution-annealed condition which provides a coarse grain structure for the best creep-rupture strength. It is further strengthened by precipitation of carbides such as MC, M_6C (rich in Ni and Mo), and $M_{23}C_6$ (rich in Cr).

Reports on the corrosion behavior of alloy 617 exposed to SCW are very limited. Steam oxidation studies of alloy 617 indicated that Cr_2O_3 and $MnCr_2O_4$ formed on the surface within a short period of time (e.g. ~1000 hrs) and additional NiO formed after a longer exposure at 800 °C and 4 MPa [22]. Alloy 617 exposed to moist air (3% water) at 700 °C followed a parabolic rate law [23]. The corrosion resistance of alloy 617 was found inappropriate for the very high temperature reactor nuclear application [24]. Based on our previous work on the GBE of alloy 800H, which demonstrated significant improvement on oxide stability by GBE during exposure to supercritical water [25], the GBE approach was investigated for alloy 617 in this study to improve its corrosion resistance.

1.4.3. Ferritic/martensitic steel HCM12A

Ferritic/martensitic (F/M) steels have been widely studied and developed for applications in the energy industry. Their performances in various energy systems had been reviewed by Klueh and Harries [26]. In this alloy family, alloy HCM12A (12Cr-2W-0.4Mo-1Cu-V,Nb) is one of the third generation 12Cr ferritic steels with tempered martensite [27], which was developed for heavy section components such as headers and steam pipes at temperatures up to 620°C and pressures up to 34 MPa [28], with good resistance to thermal shocks [29]. In addition to the improved thermal shock resistance, F/M steels have better radiation-induced void swelling

resistance compared to austenitic steels, which stimulates their applications in nuclear energy technologies [30,31]. The design of alloy HCM12A took the following several aspects into consideration. To improve weldability, the carbon content of alloy HCM12A is reduced to about half of the carbon content in conventional 12Cr ferritic steels, such as HT91 that has been extensively used as high-temperature components in power plants. W, Mo, V and Nb are added to improve the creep strength of alloy HCM12A through two strengthening mechanisms: solution strengthening by W and Mo, and precipitation strengthening by V and Nb. W strengthening is more effective for creep resistance than Mo strengthening. V and Nb produce marked effects on precipitation strengthening because they form extremely fine coherent MX carbonitride on the ferrite matrix. Cu is added in alloy HCM12A instead of Ni as an austenite-forming element to minimize δ-ferrite that is harmful to toughness. Ni content is limited in alloy HCM12A because Ni decreases the long-term strength and greatly reduces the austenite completion temperature that impairs allowable high-temperature tempering.

There are some previous oxidation studies in high-temperature steam environment [32,33,34] for the 9-12%Cr ferritic/martensitic steels including alloy HCM12A used for advanced power plants. A dual-layer oxide was observed on the surface with the outer layer being primarily composed of Fe oxide and the inner layer containing the oxides of Fe and other alloying elements. A preliminary study of oxidation resistance of alloy HCM12A exposed in water at 574°C and 19.2 MPa was reported by Sawaragi et al [35], and they also observed a dual-layer oxide formed on the surface, but no detailed information was provided. Heavy iron oxide deposits are generated inside the boiler tubes of the fossil plants operating at supercritical temperatures, and magnetite crystal growth is the dominant fouling mechanism [36]. Oxide flakes peeled from the oxide layer mix with the fluid that will flow into the turbine. The turbine blades may be subject to unbalanced forces due to uneven distribution of oxides deposited on the turbine plate. Thus, the performance of the turbine will be degraded, which eventually impairs the efficiency of power plants. To improve the corrosion resistance, the effect of GBE on the corrosion of HCM12A has been studied in this project.

1.4.4. CVD SiC

The use of SiC in commercial nuclear reactors, particularly as cladding for advanced fuels, could provide substantial safety and economic benefits. SiC possesses excellent high-temperature mechanical properties and it has been shown to be stable under neutron irradiation [37,38]. However, the stability of SiC in water coolants under typical light water reactor (LWR) operating conditions must be demonstrated before this material can be deployed in commercial water reactors.

Hydrothermal corrosion of SiC has been the subject of numerous investigations [39,40,41,42,43,44]. Of particular interest, Hirayama, et al. found that the dissolution rate of SiC in water at 290°C is accelerated by increasing pH and the amount of oxygen dissolved [39]. They also reported that the dissolution rate of SiC in an oxygenated alkaline solution follows linear kinetics whereas in an acidic solution, it approximates parabolic kinetics. Microstructural analysis revealed that corrosion occurred at the grain boundaries and that there was no evidence for the formation of a protective SiO_2 layer [40].

Kim, et al. [43,44] reported that CVD SiC exhibited better corrosion resistance than reaction-bonded SiC (RBSC) and sintered SiC (SSC) in water at 360°C, that residual free silicon in RBSC was preferentially corroded and that the kinetics of corrosion followed a parabolic law, except

for abrupt increases in weight loss after 7 and 10 days for SSC and CVD-SiC, respectively. Kim, et al. [43] also showed that the corrosion of RBSC was accelerated by increasing pH through the addition of small amounts of LiOH.

Kraft, et al. [42], observed linear corrosion behavior for CVD SiC fibers (Specialty Materials Inc, Lowell, MA) in water at 200 MPa and temperatures in the range of 400 – 700°C and concluded that no protective layer had formed on the surface of the fibers.

In this study, microstructural effects such as GBs and residual strains on the corrosion behavior of CVD SiC were investigated.

2. Experiments

2.1. Materials and sample preparation

Commercial alloys 800H, 617, HCM12A, and SiC were used in this study. The measured chemical compositions are listed in Table 1. The SiC (Rohm & Hass Company, Advanced Materials, Woburn MA) was fabricated by means of CVD. The as-received (AR) alloys 800H and 617 were solution-annealed at 1177°C and ~1170 °C for a time commensurate with section size followed by water quench, respectively. The F/M steel HCM12A was procured from Sumitomo Metal Industries, Ltd., and had been normalized at 1050°C and tempered at 770°C.

Table 1. Chemical composition (wt.%) of the as-received alloys 800H, 617, and HCM12A.

Alloy	Fe	Cr	Ni	Co	W	Mo	Mn	Cu	Si	Ti	Al	Others
800H	45.26	20.42	31.59	-	-		.76	.42	.13	.57	.50	C, S, P
617	1.47	22.05	52.32	12.69	-	9.35	.27	.11	.15	.38	1.07	C, S, B
HCM12A	84.22	10.83	.39	-	1.89	.3	.64	1.02	.27		.001	Nb, V, N, C, S, P, B

GBE was performed on some of the 800H and 617 samples in the AR conditions by means of a series of small thickness reduction (e.g. ~6%) followed by annealing at 1050 and 1100°C for 90 minutes, respectively [45,46]. Similar TMP was performed on the AR HCM12A samples with a series of small thickness reduction followed by annealing above 1000°C and fast quenching in liquid nitrogen. After the sequential TMP, the samples were tempered at 770°C to obtain the same phase components as the AR HCM12A. Average grain sizes of the GBE-treated samples were ~100 and ~25 μm for the alloys 800H and 617, respectively. The GBE treatments did not significantly change the average grain size of the alloys. Although corrosion rates have been reported to be dependent upon grain size [47], the grain size is not expected to play a role on the corrosion behavior of these studies due to the similar grain size between the AR and the GBE-treated samples.

The AR and the GBE-treated samples of these three alloys and SiC were prepared in the same size of 31.7×12.7 mm with a thickness of ~1 mm. The samples were polished down to 1 μm finish with diamond paste. Some of the AR 800H samples were subjected to a shot-peening (SP) treatment with ~500 micron diameter stainless steel beads at ~0.3 MPa for 3 seconds.

5

2.2. Tests

The corrosion/oxidation performance of the AR, GBE-treated, and SP samples was tested in supercritical water (SCW) and in cyclic oxidation conditions.

SCW, with temperature and pressure above the critical point of water at 374°C and 22.1 MPa, has been employed in modern power plants to improve thermal efficiency and reduce the release of deleterious gases. The SCW was maintained at 500 and 600°C and ~25 MPa with a dissolved oxygen content of ~25 ppb (part per billion) at the test section inlet and a flow rate of ~1 m/s during the tests. The SCW exposure experiments were performed in the University of Wisconsin SCW loop. The detailed construction and system capabilities of this SCW loop are described in Ref. [48].

Cyclic oxidation testing is a key method to aid material selection and to predict service lifetime of components. Cyclic oxidation tests were performed in air for 42 cycles with each cycle being composed of a 24 hour hold at 850°C followed by 15 minutes air cooling, with subsequent weight measurements.

2.3. Characterization techniques

The oxidation behavior of the samples was examined by means of a variety of analytical methods. An electronic balance with a measurable sensitivity of 0.1 mg was used for gravimetry. A LEO 1530 field-emission scanning electron microscopy (FESEM) incorporated with an energy-dispersive X-ray spectroscopy (EDS) system was employed for characterizing oxide morphologies, oxide layer structures, and compositional distribution. A Philips 200CM transmission electron microscopy (TEM) was used to characterize microstructure in high resolution. A STOE X-ray diffractometer was used for characterizing phases, grain size, and microstrain. A Zygo NewView 3D optical profile was used to measure the topology/roughness of the surfaces. In addition, electron backscatter diffraction (EBSD) was used to characterize the phases, GBs, and strains.

To obtain good quality EBSD patterns, the cross-section samples were polished with SiC abrasive paper to 1200 grit followed by polishing with diamond paste, alpha alumina, and colloidal silica solutions in sequence. The EBSD investigation was performed in a LEO 1530 FEGSEM incorporated with a TSL orientation imaging microscopy (OIM) system MSC2200. The SEM was operated at 20kV and the automatic EBSD area scan was performed using a hexagonal grid with small step sizes (e.g. 0.1 μm). To allow identification of the existing phases with the EBSD analytical software, crystallographic data files were established based on the XRD analyses in addition to the available database included in the software. For phase analysis with EBSD, a voting scheme and the confidence index (CI) established by TSL were used [49]. A high number of votes and higher CI values indicate a higher possibility that the phase is correctly identified.

3. Effect of grain boundaries on corrosion/oxidation

3.1. Grain boundary engineering (GBE) of the alloys 800H and 617

The GBE-treatments performed on the alloys 800H and 617 did not change the grain size and hardness of the materials as statistically measured by EBSD mapping and the Vicker's micro-

hardness. Coherent twins were not counted as grain boundaries during the grain size calculation because they are immobile and not a constituent of the intergranular transport network [45]. At the GBE treatment temperatures such as 1050 °C for the alloy 800H and 1100°C for the alloy 617, only carbides may be changed by the GBE treatments since carbides such as $Cr_{23}C_6$ start to form at temperatures below ~1100°C according to thermodynamic calculations. However, distinct thermal segregation and precipitation were not introduced by the GBE treatments as evaluated by scanning Auger microscopy analyses on in-situ fractured samples. The only significant change induced by the GBE-treatments is the GBCD.

3.1.1 Grain boundary character distribution (GBCD)

The GBCD of the AR and the GBE-treated alloys 800H and 617 samples are plotted in a triangle (an adapted ternary phase diagram) as shown in Fig. 1(a) with the three axes denoting the fraction of the $\Sigma 1$, low-Σ CSL, and general boundaries. The GBE treatment greatly increased the fraction of low-Σ CSLBs and decreased the fraction of general boundaries. The fraction of low-Σ CSLBs with Σ from 3 to 29 of the AR and the GBE-treated alloy 800H and alloy 617 samples is shown in Fig. 1(b). The fraction of annealing twin boundaries $\Sigma 3$ and its twin variants $\Sigma 9$ and $\Sigma 27$ had been greatly increased by the GBE treatment, which indicates that a lot of twinning and multiple twinning events occurred during the TMP. This is desirable for property improvement of materials [50,51]. The fraction of $\Sigma 3$ boundaries of the GBE-treated alloy 617 samples was enhanced to ~64% which is approaching the theoretical twin limit of 2/3 [52].
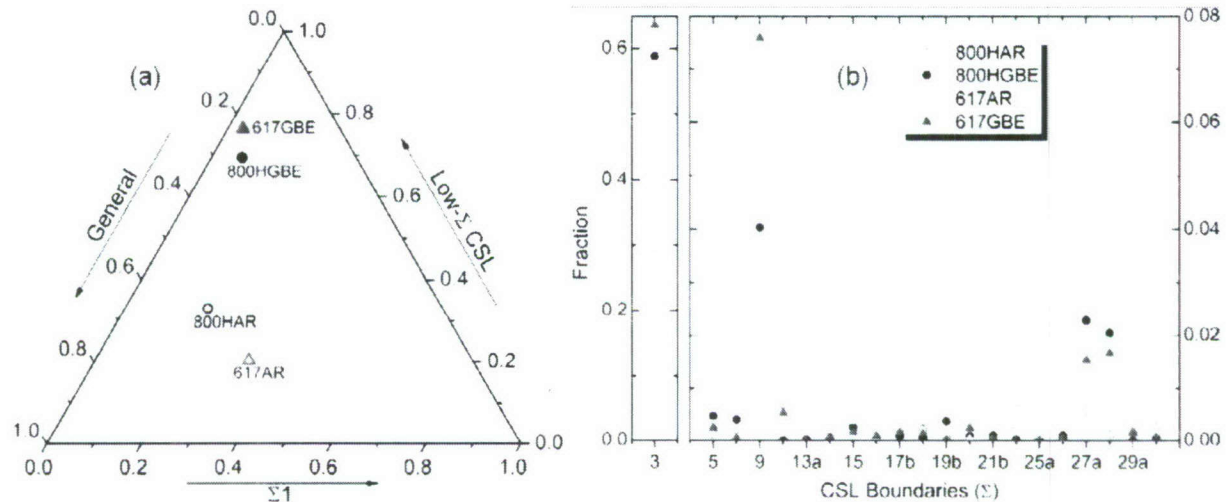

Fig. 1. (a) GBCD (fraction of $\Sigma 1$, low-Σ CSL, and general boundaries) and (b) the fraction of low-Σ CSLBs ($3 \leq \Sigma \leq 29$) of alloy 800H and alloy 617 in the AR and the GBE-treated conditions.

3.1.2 Thermal stability of the GBE-treated samples

Since atomic migration is increased at elevated temperatures, the GBE-promoted low-Σ CSLBs may become unstable and be transformed into random boundaries. Thus, it is necessary to evaluate the thermal stability of the GBE-optimized GBCD of the materials. The GBE-treated alloy 800H samples were annealed at 500, 600, and 760°C for 4 and 6 weeks. The AR samples

7

were annealed simultaneously along with the GBE samples as a reference. The GBCD of the annealed samples, which is plotted in Fig. 2(a), indicates that the GBCD was slightly changed by the anneal for both the AR and the GBE-treated samples. The anneal at 760°C (~58% melting temperature of alloy 800H) only slightly changed the GBCD of the GBE-treated samples.
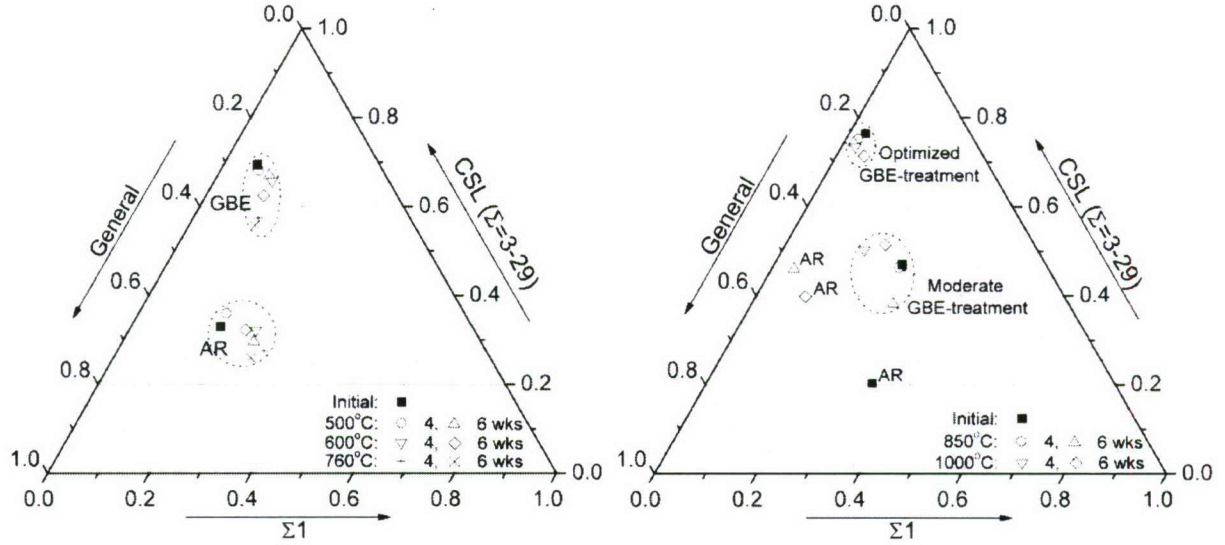

Fig. 2. Annealing effect on the GBCD (fraction of Σ1, low-Σ CSL, and general boundaries) of the AR and the GBE-treated samples of (a) alloy 800H annealed at 500, 600, and 760°C for 4 or 6 weeks and (b) alloy 617 annealed at 850 and 1000°C for 4 or 6 weeks.

Similar thermal stability testing was performed on the AR and the GBE-treated alloy 617 samples by annealing at 850 and 1000°C for 4 and 6 weeks. Samples with a moderate GBE-treatment were also tested at the same time. The GBCD of the annealed samples, which is plotted in Fig. 2(b), indicates that the GBCD of the AR samples was changed significantly compared to the GBE-treated samples. This may result from the deformation-induced texture that contributed to the statistics of the Σ1 boundaries [53,45]. The GBCD of the samples with an optimized GBE-treatment was very stable at temperatures up to 1000°C (~77% melting temperature of alloy 617) compared to that of the samples with a moderate GBE-treatment.

Therefore, the samples of alloys 800H and 617 with the optimized GBE-treatments are stable at their application temperatures up to 760°C for alloy 800H and 1000°C for alloy 617. Although the test time was limited to 6 weeks, the degradation rate of the GBCD of the optimally formed GBE-treated samples was very slow compared to the samples with moderate GBE-treatment.

3.2. Supercritical water (SCW) exposure tests

Both the as-received and the optimal GBE-treated alloy 800H and 617 samples were exposed to SCW to evaluate the GBE effect on the corrosion behavior.

3.2.1. Alloy 800H

8

After exposure to SCW at 500 and 600°C for a variety of exposure times, the surface morphology of the samples was studied with optical microscopy and SEM, the results of which are shown in **Fig. 3**. Extensive oxide exfoliation occurred on the as-received samples exposed to the SCW at 500°C for 3 weeks (**Fig. 3**(a)) and 600°C for 6 weeks (**Fig. 3**(c)). In contrast, the oxide scale is continuous and compact on the GBE-treated samples exposed to the SCW at 500°C for 4 weeks (**Fig. 3**(b)) and 600°C for 6 weeks (**Fig. 3**(d)).
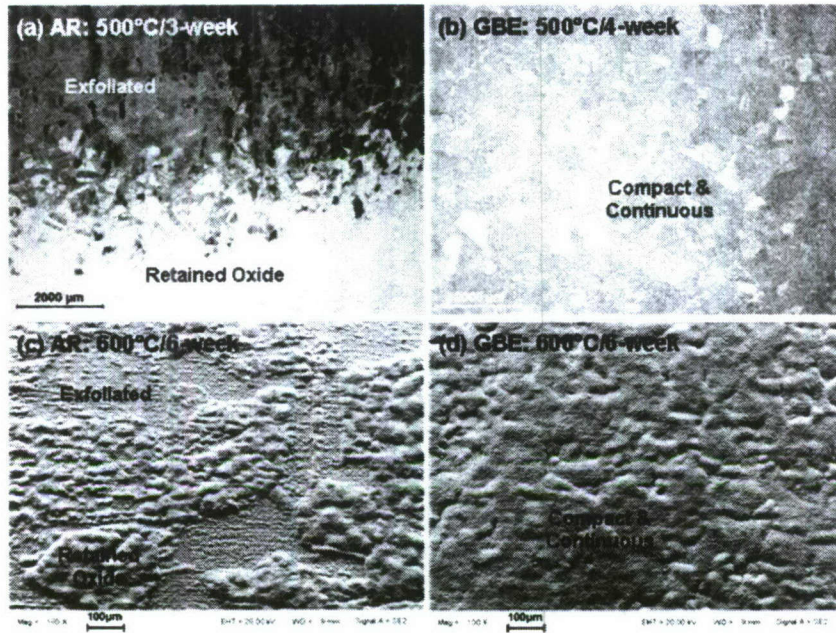
Fig. 3. Surface morphologies of the AR and the GBE-treated alloy 800H samples exposed to the SCW at 500°C for 3 or 4 weeks (a, b: optical images) and 600°C for 6 weeks (c, d: secondary electron images).

To analyze the cause of the distinct difference, cross-section samples were prepared for microstructural analysis by means of EBSD. Fig. 4 shows the EBSD maps illustrating the distribution of phases and strain in the as-received and the GBE-treated samples exposed to the SCW at 500°C for 3 weeks (Fig. 4(a) and (b)) and 4 weeks (Fig. 4(c) and (d)), respectively. Austenite (FCC structure), magnetite/spinel, and hematite were identified by the EBSD analysis as shown in Fig. 4(a). Magnetite and spinel are not differentiable by EBSD due to their identical crystal structure, but EDS analysis indicated that the inner layer is spinel and the outer layer is magnetite [25]. Compared to the as-received sample as shown in Fig. 4(a), the GBE-treated sample, as shown in Fig. 4(c), has an outer layer with a higher fraction of hematite mixed with a small amount of magnetite, and an inner layer with spinel mixed with phases identified as the austenite. The strain distribution as shown in Fig. 4(b) is presented by local average misorientation between each EBSD data point measurement and its neighbors excluding any higher angle boundaries (>5°). This figure indicates that there is a strain accumulation close to the spinel-magnetite interface (the interface between the inner and the outer layers). The strain distribution, as shown in Fig. 4(d), is relatively uniform in the oxide scale on the GBE-treated sample compared to that on the as-received sample. By integrating the strain intensity along the direction parallel to the spinel-magnetite interface, relative strain intensity as a function of the

location across the oxide scale was obtained and is plotted in Fig. 5. It is clear that there is a sharper strain change at the spinel-magnetite interface in the as-received sample compared to that in the GBE-treated sample. The strain change at the spinel-magnetite interface on the GBE-treated sample is about ½ of that on the as-received sample. The sharper strain change in the oxide scale may have contributed to the extensive oxide exfoliation that occurred on the as-received sample.
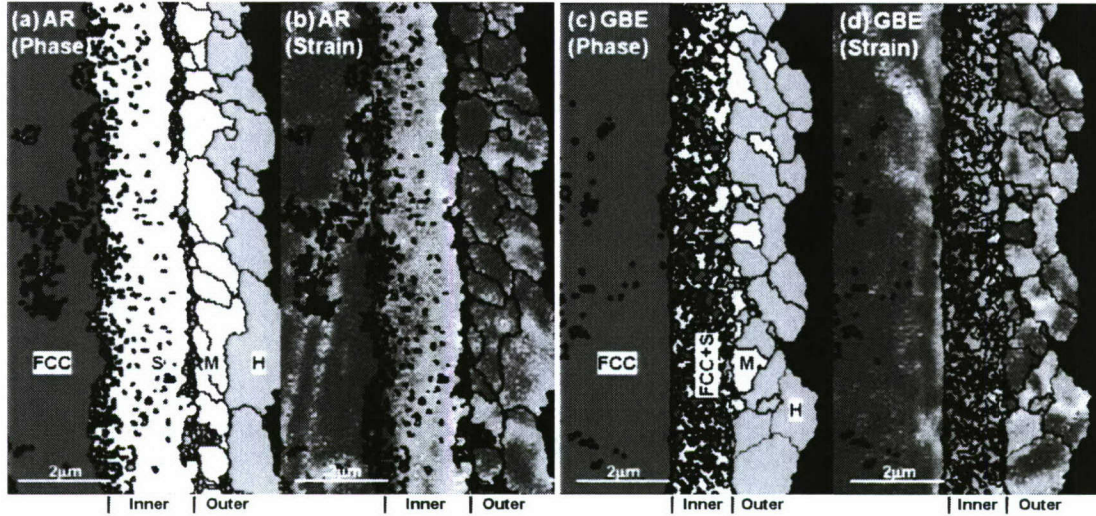

Fig. 4. EBSD maps of cross-section alloy 800H samples demonstrating the phase and strain (▨ 0° – 5° average misorientation) distribution: (a, b) the AR samples exposed to the SCW at 500°C for 3 weeks and (c, d) the GBE-treated samples exposed to the SCW at 500°C for 4 weeks. The labels FCC, S, M, and H denote phases with face-centered cubic structure such as the substrate austenite, spinel [(Fe,Cr)$_3$O$_4$], magnetite [Fe$_3$O$_4$], and hematite [Fe$_2$O$_3$], respectively.
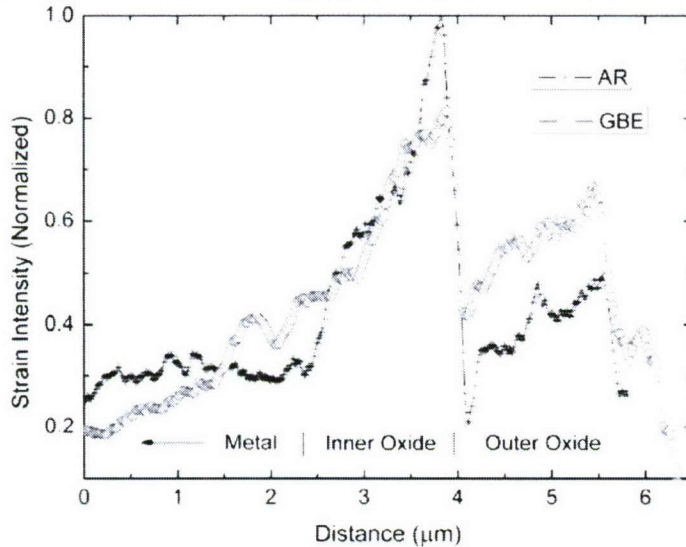

Fig. 5. Normalized strain intensity across the oxide scale on the AR and the GBE-treated alloy 800H samples as shown in Fig. 4. The two lines are aligned at the inner-outer oxide interface.

As described in the Section 3.1, the only major microstructural change induced by the GBE treatments is the greatly increased fraction of low-Σ CSLBs and decreased fraction of general boundaries. Although there is also a decrease in the fraction of $\Sigma 1$ boundaries, the effect of these boundaries on properties is smaller than the others [2]. Generally, GBs are fast diffusion paths. The low energies associated with the high population of low-Σ CSLBs do not favor fast diffusion, and thus decrease the overall diffusivity along grain boundaries, shifting the grain boundary diffusivity much closer to the bulk diffusivity. The lower global diffusivity through the sample decreased the outward transport of Fe in the GBE-treated alloy 800H sample, resulting in less Fe supplied to the GBE-treated sample surface compared to that on the as-received sample. The reduced Fe resulted in a relatively higher oxygen activity promoting the formation of hematite instead of magnetite on the GBE-treated alloy 800H sample exposed to the SCW (Fig. 4(c)) [54]. Similarly, the inward diffusivity of O was also decreased in the GBE-treated sample, resulting in less oxidation in the inner layer of the oxide scale (Fig. 4(c)).
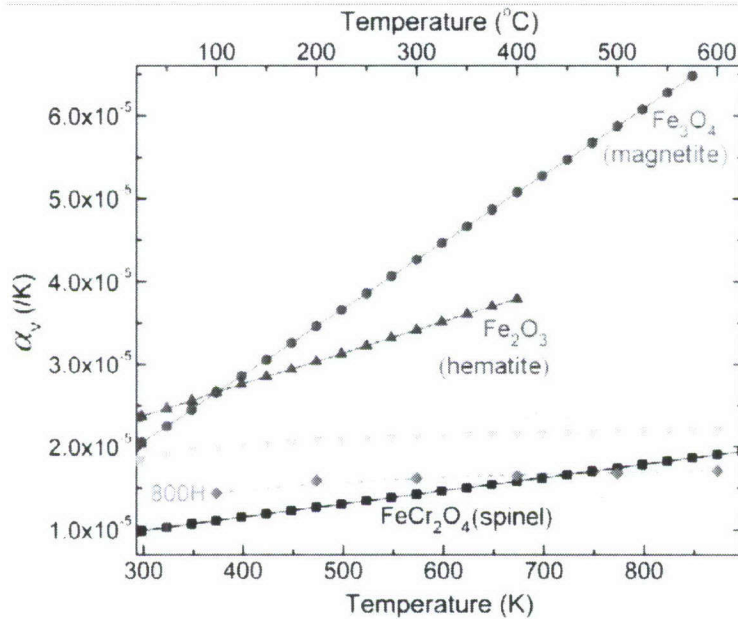

Fig. 6. Volume thermal expansion coefficient (α_v) of alloy 800H [14] and oxides such as Fe_2O_3 (hematite), Fe_3O_4 (magnetite), $FeCr_2O_4$ (spinel), and Cr_2O_3 (eskolaite) [55].

Fig. 6 shows the volume thermal expansion coefficient (α_v) of alloy 800H [14] and the specific oxides hematite, magnetite, and spinel [55]. The pressure effect on the thermal expansion coefficient is negligible due to the relatively low testing pressure (~25 MPa) and the similar bulk modulus of these oxides [56,57,58]. The α_v coefficients of hematite and spinel decrease with a similar trend in transitioning from the testing temperature to room temperature. However, the trend of the α_v of magnetite becomes significantly different from that of spinel and hematite for temperatures below ~400 °C. The significant difference in the α_v coefficients of magnetite and spinel may have led to the sharper strain change at the spinel-magnetite interface on the as-received sample (Fig. 4(b) and Fig. 5). While the smaller α_v difference between

11

hematite and spinel as well as the decreased fraction of spinel may have alleviated the strain at the spinel-hematite interface on the GBE-treated sample (Fig. 4(d) and Fig. 5). Furthermore, hematite has a higher thermal conductivity (12.6 W/m-K) than magnetite (5.0 W/m-K) [59], which more rapidly dissipates heat and results in a higher strain intensity in the outer layer (hematite). This increased strain intensity in hematite further decreased the strain change at the inner-outer interface (the spinel-hematite interface) on the GBE-treated sample (Fig. 5). The strain distribution (Fig. 5) and the α_v of the oxides (Fig. 6) support the experimental observations that the oxide exfoliation occurred mostly at the spinel-magnetite interface with a few at the magnetite-hematite interface in the as-received samples.

In addition to the sharper strain change, strong and anisotropic texture was observed in the oxide scale on the AR sample [25]. The maximum texture intensities of magnetite/spinel and hematite on the 3-week exposed AR and 4-week GBE-treated samples along the TD [010] and RD [100] directions are plotted in Fig. 7. The AR sample (3C) had stronger texture than the GBE-treated sample (4G), and the hematite texture was greater than the magnetite/spinel texture. For the 3C sample, the texture along the RD [100] direction was stronger than that along the TD [010] direction, especially for hematite texture in which the texture intensity along RD [100] direction was about three times of that along TD [010] direction. In contrast, the texture intensity along the RD [100] and TD [010] directions for the 4G sample was similar. These results indicate that the oxide formed on the AR sample was more anisotropic than that in the GBE-treated 4G sample. The anisotropic texture may result from the anisotropic energies of GBs [60,61], which is related to growth stress (intrinsic stress) [62]. GBE tuned the GBCD and the grain boundary energy distribution. GBs with relatively isotropic energy may be promoted after TMP, which results in an oxide growth favoring improved exfoliation resistance [25].
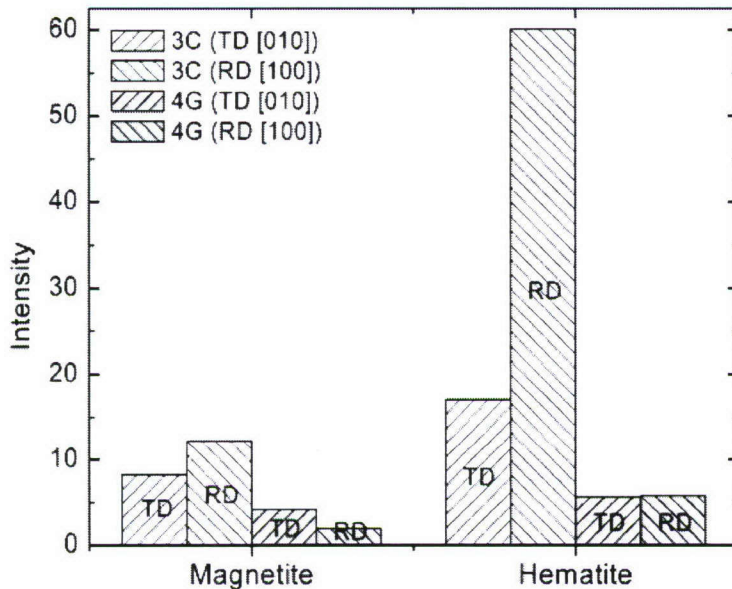

Fig. 7. Maximum texture intensity (defined as the ratio of measured to random orientation) of magnetite and hematite on 3-week SCW-exposed AR (3C) and 4-week exposed GBE-treated (4G) samples along the direction parallel to oxide growth (TD [010]) and oxide surface (RD [100]).

3.2.2. Alloy 617

The oxide scale formed on the SCW-exposed alloy 617 samples is less than ~100 nm. It is difficult to tell the thickness difference of the scales on the as-received and the GBE-treated samples from cross-section SEM analyses. Due to the thin oxide scale, grazing-incidence X-ray diffraction (GIXRD) was employed to identify the oxide phases. The GIXRD spectra of the as-received and the GBE-treated alloy 617 samples exposed to the SCW at 500°C for 4 weeks are shown in Fig. 8, where "A" denotes FCC phase from the substrate, "C" denotes chromium oxide (Cr_2O_3, PDF# [38-1479]), and the unlabeled peaks denote spinel such as $(Ni,Co)Cr_2O_4$ (PDF# [23-1271] and [22-1084]). It is clear that oxide scales formed on both of the as-received and the GBE-treated samples are composed of chromium oxide and spinel. By comparing the relative peak intensity of the chromium oxide and the spinel, it is possible to deduce that the oxide scale on the GBE-treated sample has a higher fraction of chromium oxide than that on the as-received sample. Additionally, the GBE-treated sample shows a {111} texture in the substrate, which may have played a role on the oxide formation. The relationship between texture and grain boundary engineering has been briefly introduced in Ref. [63].
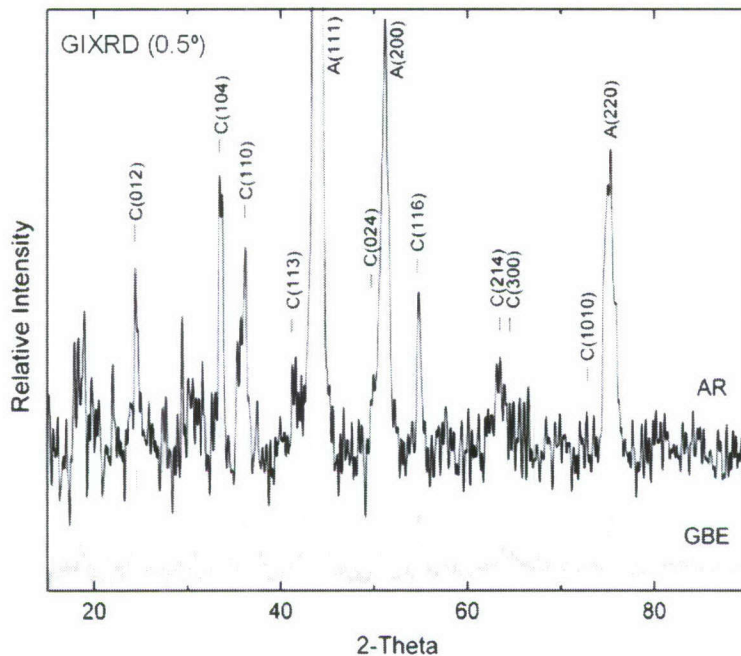

Fig. 8. Grazing incidence X-ray diffraction (GIXRD) patterns with an incident angle of 0.5° of the AR and the GBE-treated alloy 617 samples exposed to the SCW at 500°C for 4 weeks.

Oxide surface chemistry of the SCW-exposed alloy 617 samples was analyzed by XPS instead of EDS due to the thin oxide scale. XPS surface survey profiles of the as-received and the GBE-treated samples are shown in **Fig. 9**. It is clear that Ni and Co are present on the as-received sample surface in addition to Cr and O on both the as-received and the GBE-treated sample surfaces. The other peaks correspond to Auger peaks and contaminants such as C and Ar. The presence of the Ni and Co on the as-received sample surface indicates that the oxide scale on the as-received sample is either composed of a discontinuous chromium oxide or complex oxides.

13

In contrast, the GBE-treated sample surface is covered by a continuous chromium oxide. This observation is consistent with the GIXRD results as shown in Fig. 8 that the oxide scale on the GBE-treated sample has a higher fraction of chromium oxide than that on the as-received sample.
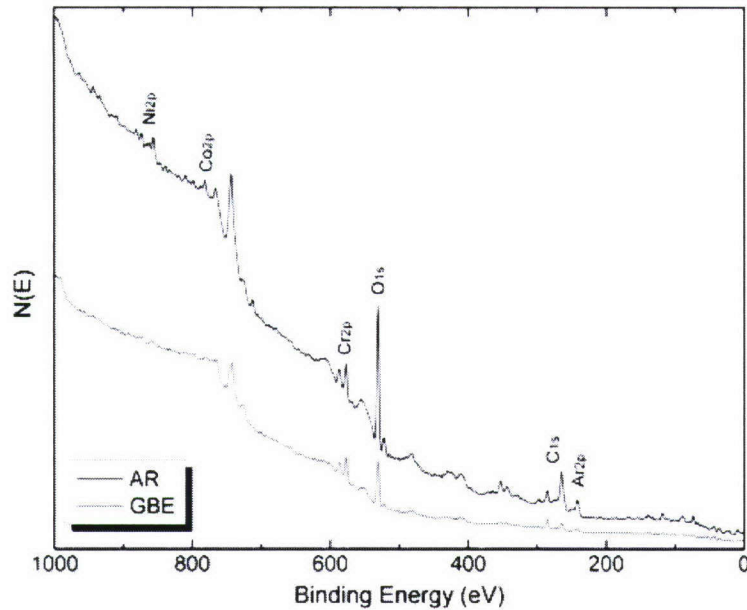

Fig. 9. X-ray photoelectron spectroscopy (XPS) surface survey spectra of the AR and the GBE-treated alloy 617 samples exposed to the SCW at 500°C for 4 weeks.

In Alloy 617, chromium was preferentially oxidized on the surface due to its higher concentration, higher diffusivity [64,65], and strong affinity for oxygen. As discussed in the previous section, the grain boundary diffusivity is expected to be much closer to the bulk diffusivity in the GBE-treated samples, which may have led to a relatively uniform diffusivity to the free surface. The uniform diffusion may have contributed to the formation of a continuous chromium oxide on the GBE-treated sample.

3.2.3. *Effect of thermomechanical processing on the corrosion of HCM12A*

The weight change of the AR and the TMP HCM12A samples exposed to the SCW at 500°C is shown in **Fig. 10**. The weight change of the AR samples approximately followed a parabolic rate law ($a = 2.16$) with a good fitting confidence ($R^2 = 0.97$). The fitting result indicates that the TMP samples followed a parabolic rate law ($a = 1.98$) with a slightly smaller rate constant compared to the AR samples. But the fitting confidence of the TMP samples ($R^2 = 0.66$) is not as good as that of the AR samples. This is mainly due to the 6-week (1026 hrs) data, which was put at a location closer to the inlet of the SCW. Although the inlet oxygen concentration was controlled at 25 ppb, the oxygen concentration was decreased from the inlet to the outlet as the oxygen consumed by the testing samples. The 6-week sample was taken out of the SCW loop with the 2-week sample to get an additional 2-week data, which is surrounded by a dashed circle. The big difference (~0.5 mg/cm^2) between the two 2-week data is believed to be mainly due to

14

the sample location with different oxygen concentration. If the big difference generated during the 2-week exposure is subtracted from the 6-week data, the revised data set can be fitted with a function of $w^{1.98} = 0.00309 \times t$, which has a highly improved fitting confidence ($R^2 = 0.90$). The revised data have the same rate law ($a = 1.98$) as the raw data but a slightly smaller rate constant. Longer exposure up to ~18 weeks is being performed to study the long-term effect of the TMP on the oxidation performance.
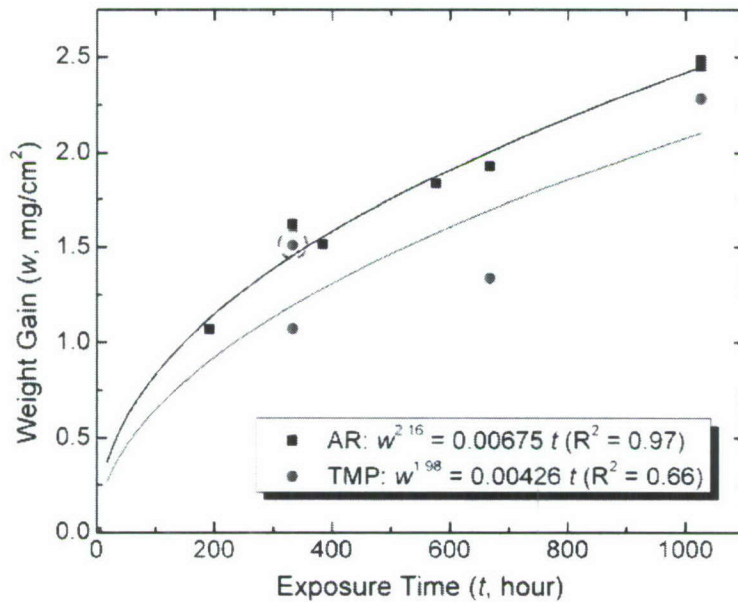
Fig. 10. Weight change (w) as a function of exposure time (t) of the AR and the TMP HCM12A samples exposed to the SCW at 500°C with a dissolved oxygen concentration of 25 ppb.
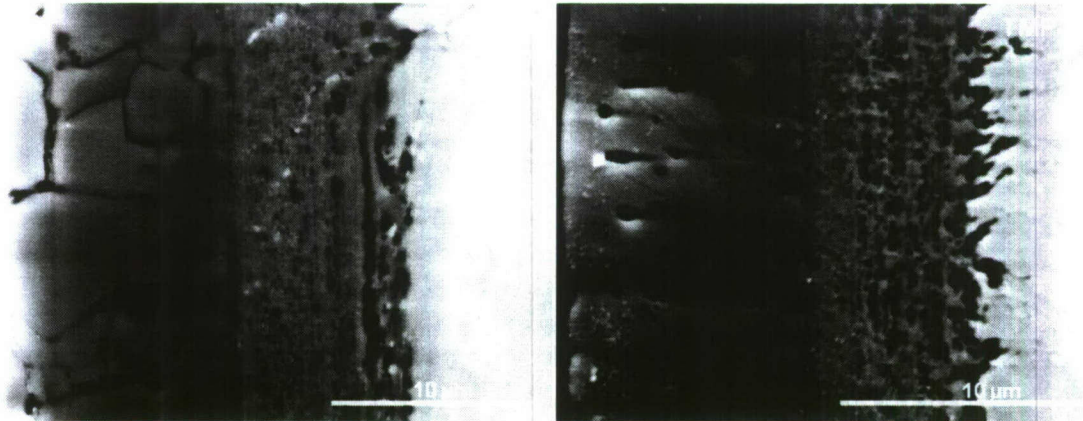

Fig. 11. Cross-sectional SEM images of the AR and the TMP samples exposed to the SCW at 500°C for ~6 weeks.

The surface morphologies of the AR and the TMP samples are not shown here due to their similarity. The cross-section samples exposed to the SCW at 500°C for ~6 weeks are shown in

Fig. 11. The figure shows that the TMP sample has a slightly thinner oxide scale than the AR sample, which is consistent with the weight gain as shown in Fig. 10. Intergranular cracks and some pores are shown in the magnetite layer on the AR and the TMP samples, respectively. A thicker and notable internal oxidation (diffusion) layer is exhibited on the TMP sample compared to the AR sample. Many nano-pores exist in the spinel layer on both the AR and the TMP samples as illustrated in the high-magnification SEM and TEM images shown in **Fig. 12**.
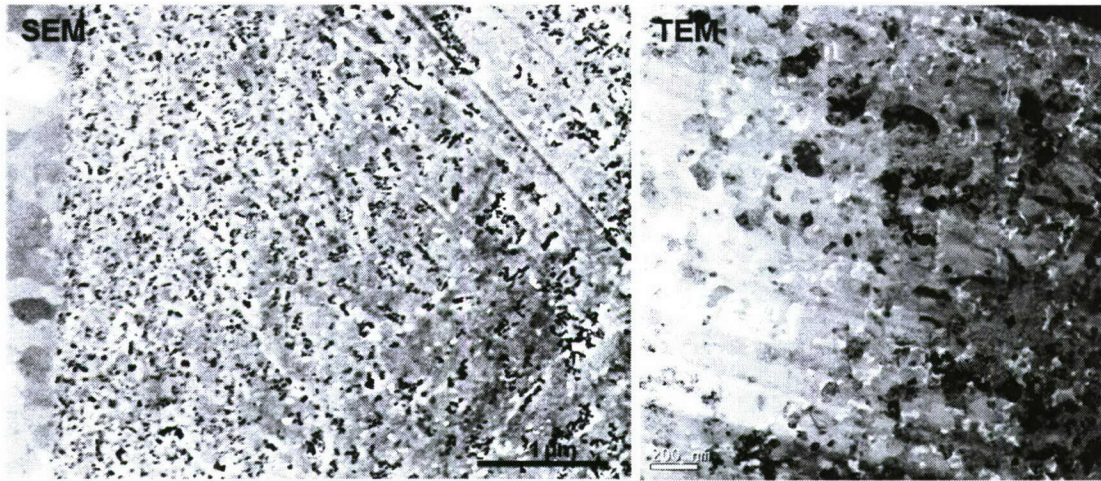

Fig. 12. SEM and TEM images of the morphologies of the inner (spinel) layer formed on the SCW-exposed HCM12A sample.

The microstructure of the oxide scales were analyzed by EBSD and are shown in **Fig. 13**. The image quality (IQ) of the two samples indicates the detailed grain structure, which is usually not able to be revealed by conventional SEM analysis as shown in Fig. 11. The IQ is very poor (dark) at GBs and pores due to the presence of defects at these features. The inner (spinel) layer with a poor IQ that results from the high density of nano-pores in this layer as shown in Fig. 12. The gradient in darkness of the spinel layer indicates that the density of the defects (nano-pores) was increased from the metallic substrate to the interface of the spinel and the magnetite layers. The internal oxidation (diffusion) layer with a lighter darkness compared to the spinel layer is observable in the IQ figures. It is clear that the magnetite layer on the TMP sample has much smaller grains compared to that on the AR sample, especially for the grains close to the spinel-magnetite interface. In addition, the shape of the small grains is more equiaxial on the TMP sample compared to the more columnar-like grains on the AR sample. The phase-orientation figures indicate that the presence of magnetite/spinel (green) and ferritic substrate (red). The variation of the color contrast indicates the (101) orientation as a function of the oxide growth direction with a lighter contrast close to the oxide growth direction.
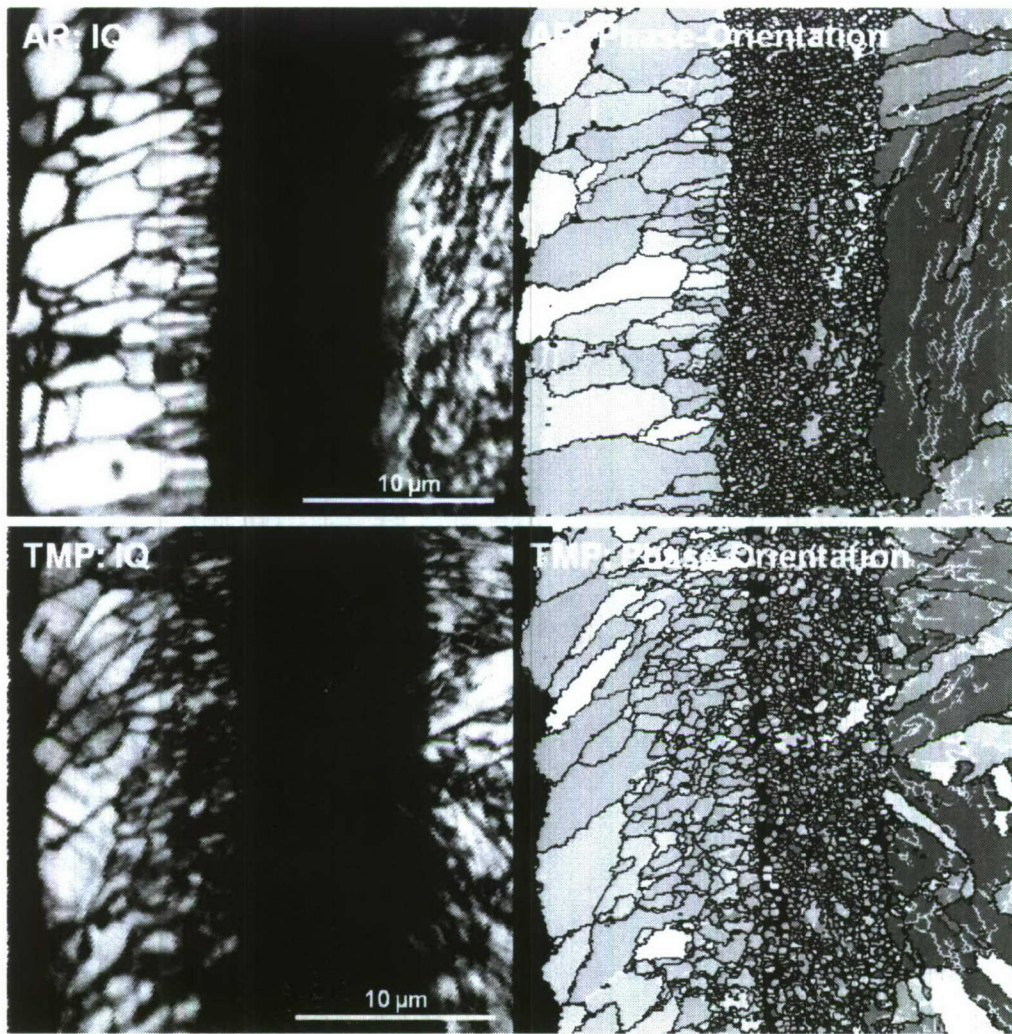
Fig. 13. EBSD maps of the AR and the TMP samples exposed to the SCW at 500°C for ~6 weeks. IQ refers to image quality of the EBSD data. Red and green corresponds to ferrite and magnetite/spinel, respectively. The variational contrast of the red and green corresponds to the (101) orientation as a function of the growth direction of the oxide scale. The lighter the color indicates the (101) texture is more close to the growth direction. The blue and white curves correspond to $\Sigma 3^n$ ($\Sigma 3$, $\Sigma 9$, and $\Sigma 27$) and low-angle boundaries, respectively.

The textures of the magnetite, spinel, and metallic substrate for the as-received and the TMP samples are shown with inverse pole figures (IPF) in **Fig. 14**. A strong (101) texture exists in the metallic substrate. The (101) texture was retained in the spinel layer but not transferred into the magnetite layer in the direction of the oxide growth. A (115) texture in the spinel layer and (525), (112), and (001) textures in the magnetite layer were formed along the oxide growth direction. Compared to the as-received sample, the strong (101) texture was modified into a near (101) texture in the metallic substrate by the thermomechanical processing. The near (101) texture was changed to (101) texture with a mild (111) texture in the spinel layer. A stronger (001) texture with a mild (535) texture were formed along the oxide growth direction in the magnetite layer.
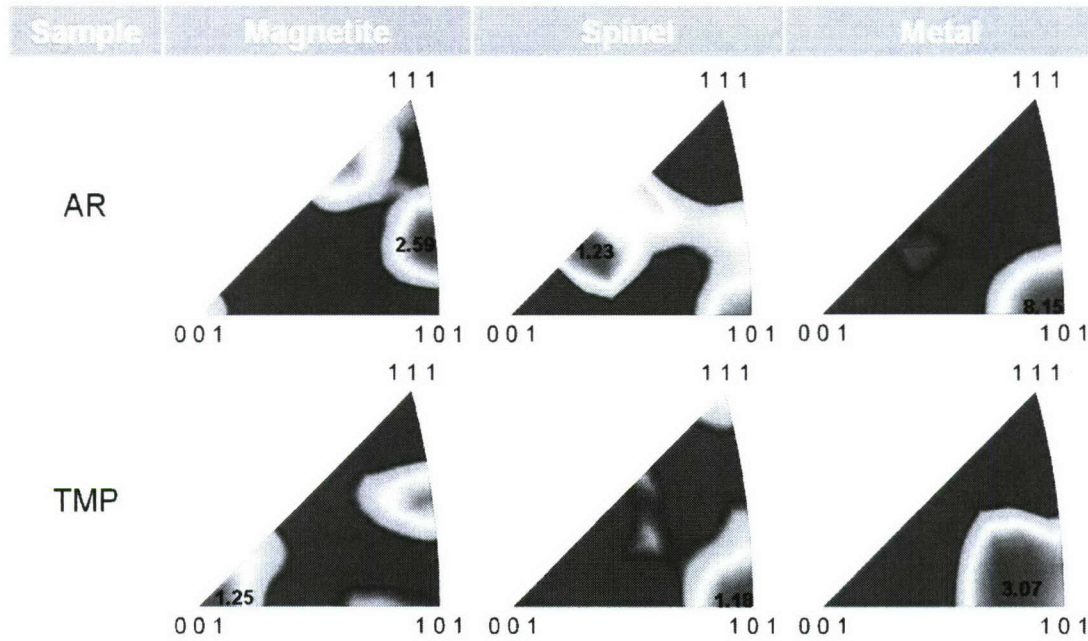
17

Fig. 14. Inverse pole figures indicating the textures of the oxides growth on the AR and the TMP samples exposed to the SCW at 500°C for ~6 weeks.

3.3. Cyclic oxidation tests

The weight changes of the as-received and the GBE-treated alloy 800H samples subjected to cyclic oxidation tests in air at 500 and 850°C for a total cyclic exposure time of 1008 hours are shown in Fig. 15. The 500°C test results as shown in Fig. 15(a) indicate that the GBE-treated samples had a weight gain, which was kept relatively constant with the cycles. In contrast, the as-received samples had a weight loss. The 850°C test results as shown in Fig. 15(b) indicate that both the GBE-treated and the as-received samples had a short period of weight gain followed by a weight loss during the rest of the cyclic exposure testing. The weight loss of the GBE-treated samples was only ~40% of the as-received samples. More extensive exfoliation was observed on the as-received samples by SEM analyses. The cyclic oxidation test results indicate that the oxide exfoliation resistance of alloy 800H was greatly improved by the GBE-treatment.

Similarly, the weight change of the as-received and the GBE-treated alloy 617 samples subjected to cyclic oxidation testing in air at 850 and 1000°C for a total cyclic exposure time of 1008 hours are shown in Fig. 16. The 850°C test results as shown in Fig. 16(a) indicate that the GBE-treated samples had a small weight gain and the weight gain was kept relatively constant with the cycles. In contrast, the as-received samples had a large weight gain, which is about 3 times that of the GBE-treated samples, at the beginning part of the cyclic oxidation test, and the weight gain decreased with the cycles. The 1000°C test results as shown in Fig. 16(b) indicate that both the GBE-treated and the as-received samples had a weight gain, but the weight gain of the GBE-treated samples was ~55% of the as-received samples. Exfoliation was only observed

18

on the as-received alloy 617 samples cyclically exposed at 850°C. The cyclic oxidation test results indicate that the oxide scale stability (relatively constant weight change) was greatly improved and the oxidation rate (weight gain) was greatly decreased by the GBE-treatment for alloy 617.
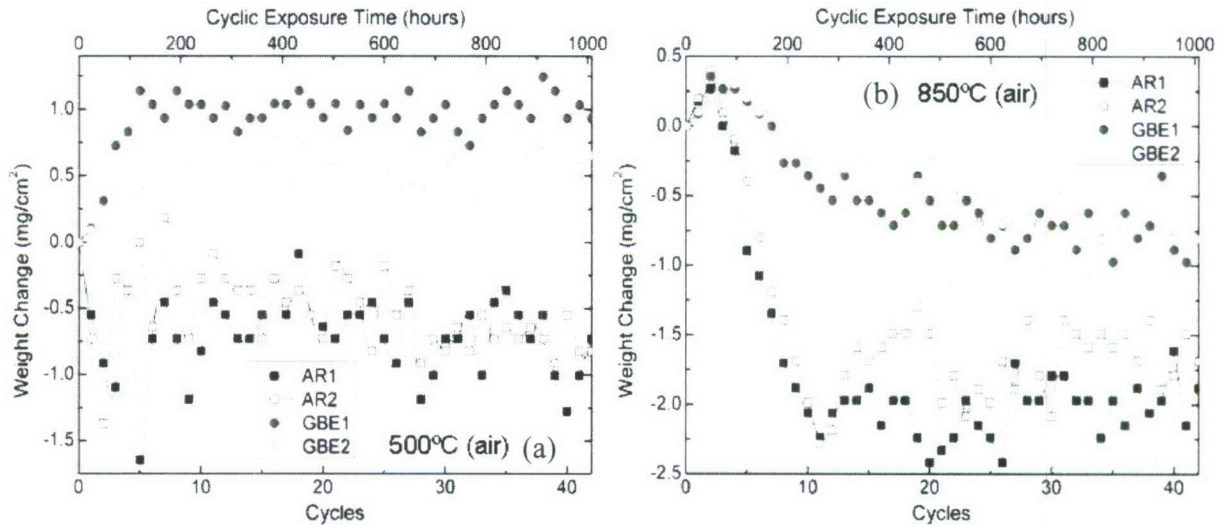

Fig. 15. Weight change of the AR and the GBE-treated alloy 800H samples subjected to cyclic exposure in air at (a) 500°C and (b) 850°C.
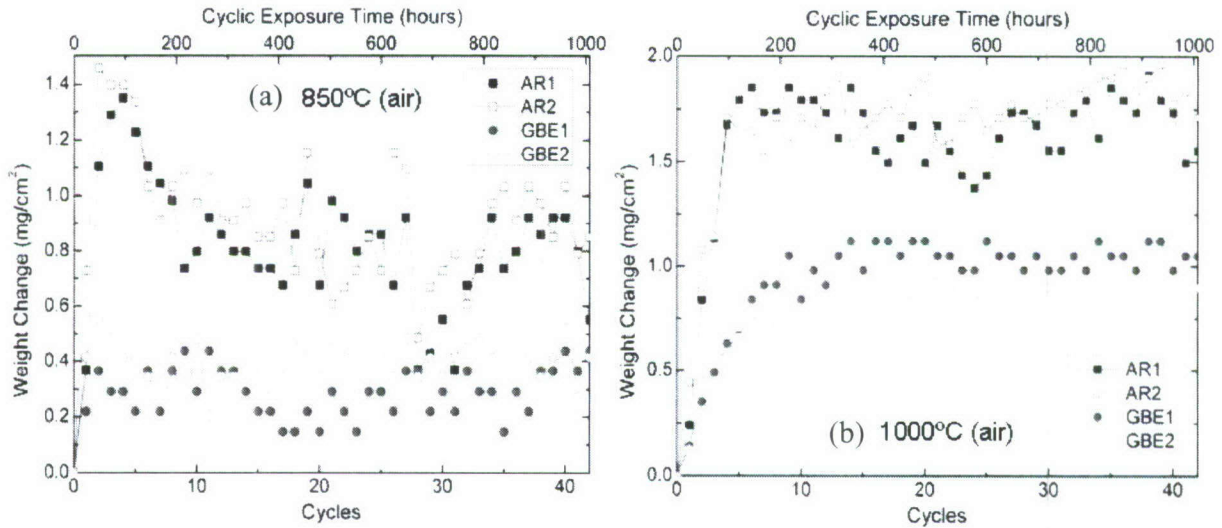

Fig. 16. Weight change of the as-received (AR) and the GBE-treated alloy 617 samples subjected to cyclic exposure in air at (a) 850°C and (b) 1000°C.

It is clear that the GBE-treatments played a significant effect on the cyclic oxidation performance of these two alloys. The microstructure of the cyclic oxidation-induced oxide scales on the as-received and the GBE-treated alloy 800H and alloy 617 samples are currently being studied and will be reported in future detailed work.

4. Effect of grain size on corrosion/oxidation

4.1. SCW exposure tests

Shot peening was used to crate small grains at the sample surface of 800H. The weight change of the AR and SP samples exposed to SCW is shown in Fig. 17. A large weight gain variation was observed for the AR samples. In contrast, the limited weight gain data of the SP samples approximately follows a linear rate law and the weight gain is only about 1/10 of the AR samples. Longer SCW exposure testing (up to 3000 hrs) is being performed to understand the trends.
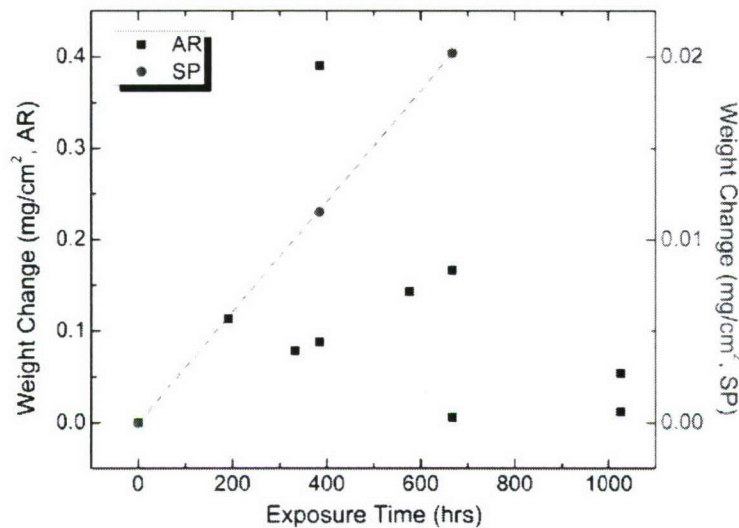

Fig. 17. Weight change of the AR (solid squares) and the shot-peened (SP, solid circles) samples subjected to the SCW exposure at 500°C.

X-ray diffraction in grazing-incidence mode (0.5°) and conventional mode (θ-2θ) was used to characterize the grain size and microstrain in the surface of the SP samples by using the Williamson-Hall method [66]. The analyzed results of the SP and the SCW-exposed SP (SP-SCW) samples are summarized in Table 2. Based on the X-ray attenuation in alloy 800H, the analytical depths of the grazing-incidence mode and the conventional mode are ~31 nm and ~4.6 μm, respectively. The results indicate that the shot-peening performed on the alloy 800H resulted in a nano-crystalline surface. The grain size decreases and the microstrain increases approaching the surface. The SCW exposure resulted in some grain growth and strain alleviation.

Table 2. Grazing-incidence (0.5°) and conventional (θ-2θ) X-ray diffraction of the shot-peened (SP) and the SCW-exposed shot-peened (SP-SCW) alloy 800H samples.

XRD	Analyzed Depth (nm)	SP		SP-SCW	
		Grain Size (nm)	Strain (%)	Grain Size (nm)	Strain (%)
GI (0.5°)	~31	15	0.39	55	0.23
θ-2θ	~4600	21	0.31	1231	0.003

20

The surface morphologies of the SP samples prior to and after the SCW exposure and the AR sample after the SCW exposure are show in Fig. 18. The secondary electron images show many dimples on the SP sample surface (Fig. 18 a) and some dimples are overlapped introducing cracks (Fig. 18 b). The SCW-exposed SP sample surface shows a fine compact oxide scale with a small amount of large oxide particles sparsely distributed close to the cracks (Fig. 18 c). In contrast, the AR sample after the same period of SCW exposure is uniformly covered with large oxide particles (Fig. 18 d).
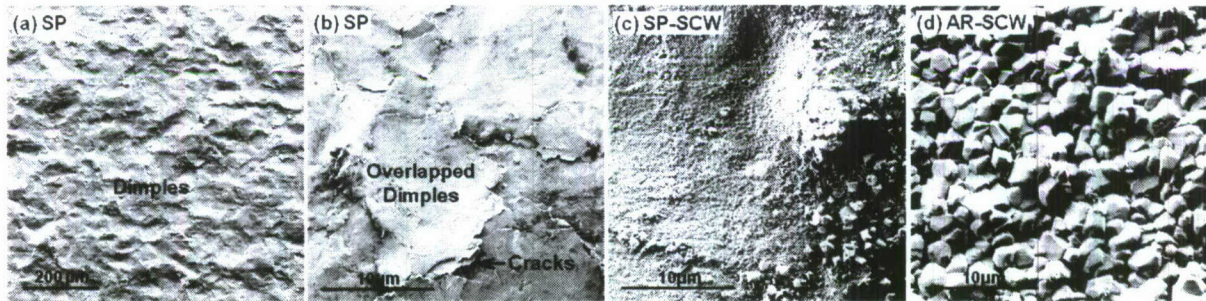

Fig. 18. Surface morphologies of the SP samples prior to (a and b) and after the SCW exposure (SP-SCW, c) and the AR samples after the SCW exposure (AR-SCW, d). (SCW: 500°C, 667 hrs)
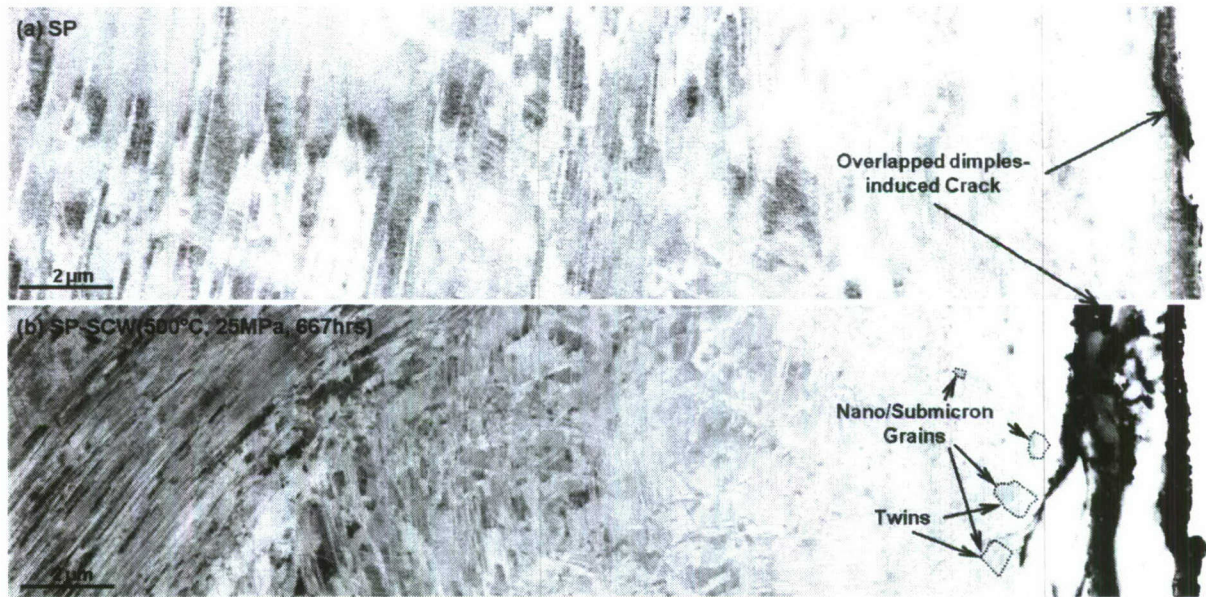

Fig. 19. Secondary electron images of cross-sectional SP samples (a) prior to and (b) after the SCW exposure at 500°C for 667 hrs. (Metal substrate on the left side)

Following peening, a deformation zone depth of ~70 μm was observed on the surface of the SP sample. The fine microstructures of the SP samples prior to and after the SCW exposure are shown in Fig. 19. The secondary electron images of the cross-sectional samples indicate that the

21

shot-peened surface is composed of two microstructure regions: an ultra-fine grain region at the surface and a sequential transition region at the subsurface, where many slip bands were observed. This is consistent with the observation on a shot-peened low-carbon steel analyzed by positron lifetime spectroscopy [67]. Surface cracks induced by overlapped dimples were also observed, which usually have a penetration depth of ~1 μm. After the SCW exposure, noticeable grains and twins in nano and sub-micron size were observed close to the surface (Fig. 19 b). In addition to the thin oxide scale formed on the surface (~0.5 μm), oxidation also occurred along the cracks and resulted in a thicker oxide scale compared to that at the surface (Fig. 19 b). The cracks induced by the overlapped dimples did not deteriorate the overall oxidation performance of the SP samples within the period of the SCW exposure.

Additional morphologies of the oxide scales formed on the SP samples exposed to the SCW at 500°C for 667 hrs are shown in Fig. 20. Fig. 20 (a) and (b) exhibit compact and continuous oxide scales on the surfaces with a large open crack and a small close crack induced by the overlapped dimples, respectively. Oxide freely formed inside the large open crack as that on the surface. In contrast, oxidation was suppressed inside the small close crack. In addition to the compact oxide scale, porous/cracked oxide scales were observed on the SCW-exposed SP samples as shown in Fig. 20 (c) and (d).

The oxide scales formed on the SCW-exposed AR and SP samples were analyzed by EDS mapping. The EDS maps of the major components such as O, Fe, Ni, and Cr and corresponding secondary electron images of the AR and the SP samples are shown in Fig. 21. The thickness of the oxide scales on the AR and the SP samples is ~3-4 μm and ~1-2 μm, respectively. The EDS maps indicate that the oxide scale on the AR sample is composed of two layers: an outer iron oxide and an inner Ni-Cr and Fe-Cr spinel (Fig. 21 a). Chromium is slightly enriched at grain boundaries and some domains in the inner layer (low contrast in the secondary electron image, Fig. 21 a). Compared to the AR sample, the oxide scale on the SP sample is also composed of two layers. By associating the EDS maps with the grazing-incidence diffraction result, the oxide scale is identified as an outer Cr-rich spinel and an inner Cr oxide. A slight Ni-enrichment in the metal was observed beneath the oxide scale (high contrast in the secondary electron image, Fig. 21 b).
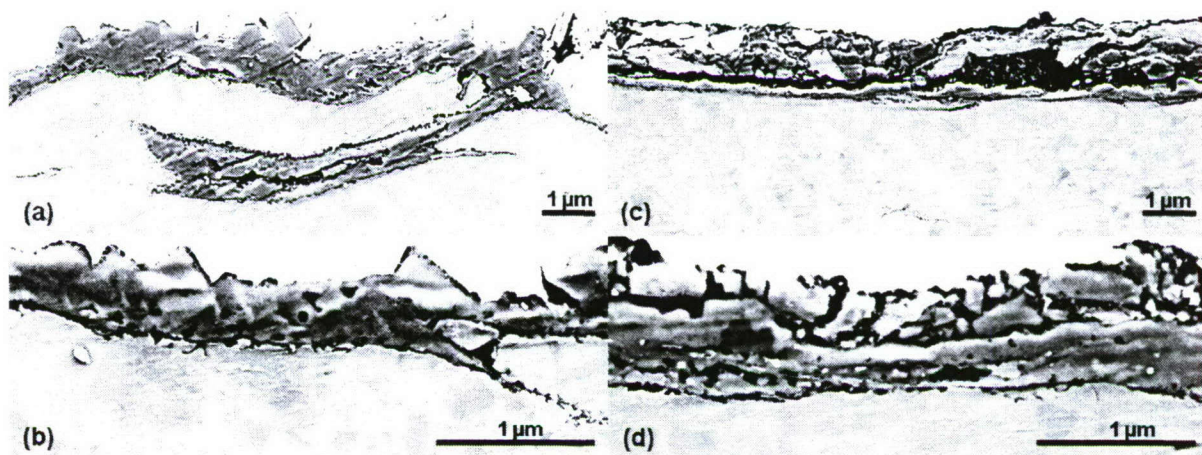

Fig. 20. Morphologies of the oxide scales formed on the SP samples after the SCW exposure at 500°C for 667 hrs.
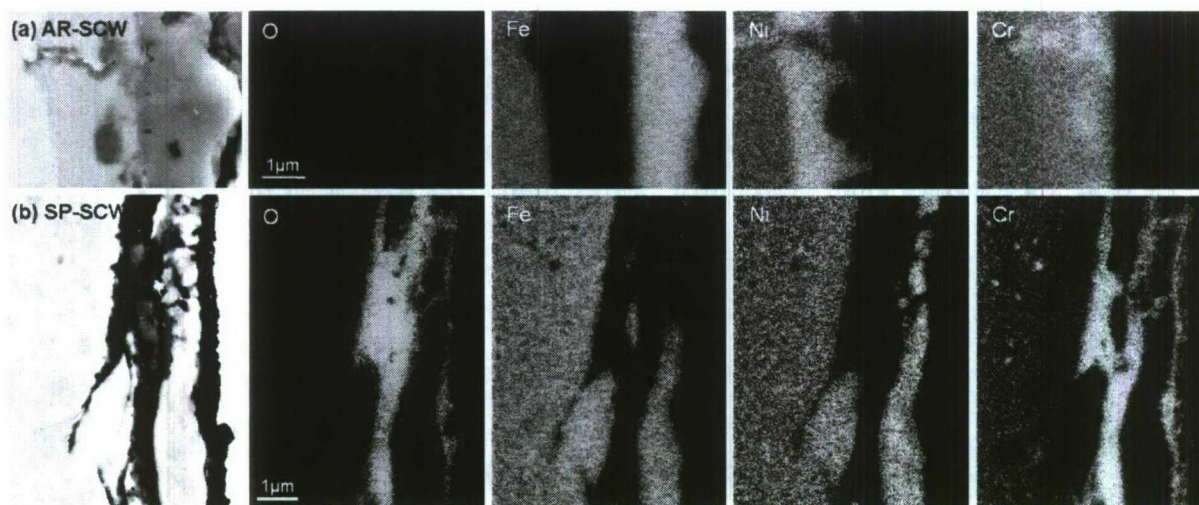
Fig. 21. EDS mapping of the cross-section samples of (a) the AR and (b) the SP samples subjected to the SCW exposure at 500°C for 667 hrs. (Metal substrate on the left side)

4.2.   Cyclic oxidation tests

Fig. 22 shows the weight change as a function of the number of cycles and the cyclic exposure time of the AR and the SP samples. The AR samples had a small weight gain in the first couple of cycles and then changed to a large weight loss. The weight loss was relatively constant at ~2 mg/cm^2 after ~10 cycles. In contrast, the SP samples had a small weight gain, which approximately follows a logarithmic rate law of $x = 0.1 \times \ln(t + 0.69) + 0.04$ with a fitting confidence of $R^2 =0.62$.
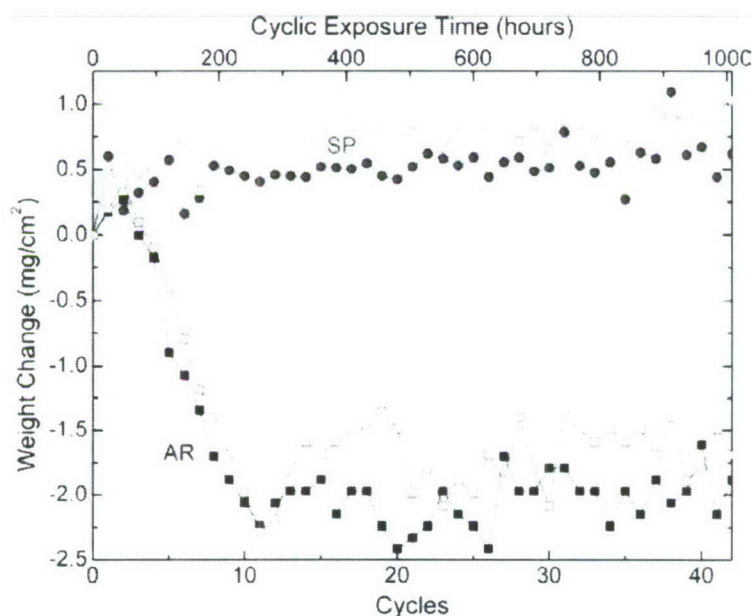

Fig. 22. Weight change of the AR and the SP samples subjected to cyclic exposure at 850 °C.

The surface morphologies of the AR and the SP samples after cyclic oxidation in air at 850°C are shown in Fig. 23. The secondary electron images show that lots of cracked bubbles and flakes exist on the AR sample but only a few exfoliations occurred on the SP sample. The surface with cracked bubbles is consistent with the observation of an as-received alloy 800H exposed to air at 800°C for 400 hours [68]. The surface morphology development contributed to the weight change of the samples as shown in Fig. 22.
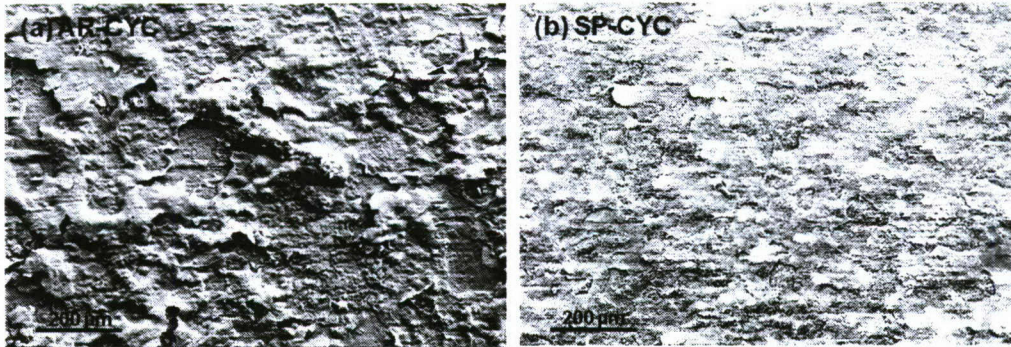

Fig. 23. Surface morphologies of (a) the AR and (b) the SP samples after the cyclic exposure testing at 850 °C.

EDS mapping of the AR and the SP cross-sectional samples is shown in Fig. 24. The secondary electron images show that the oxide thickness on the SP sample is about half of that on the AR sample. The oxide scale on the AR sample is composed of a layer enriched with Cr-Mn adjacent to metal followed by layers enriched with Ni-Fe, Ti, and Fe in sequence. Compared to the AR sample, the oxide scale on the SP sample is composed of a layer enriched with Cr-Ti adjacent to the metal followed by layers enriched with Ti and Mn-Cr-Fe in sequence.
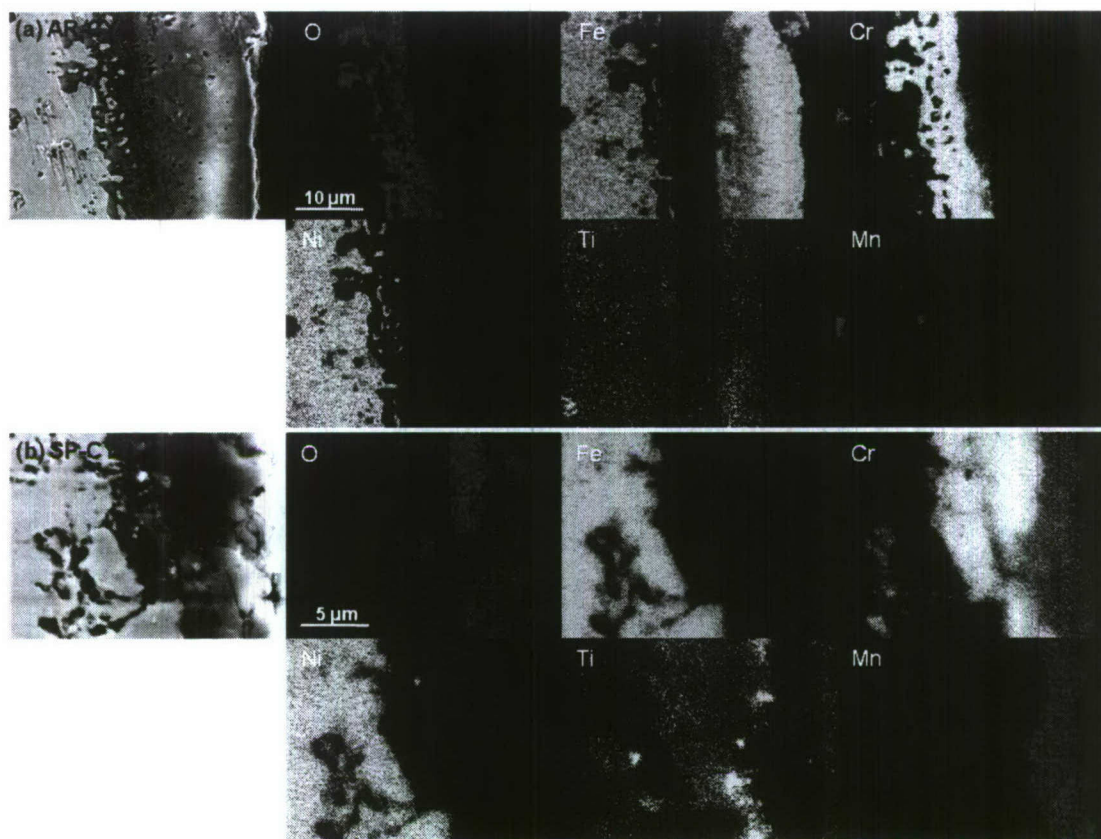
Fig. 24. EDS mapping of the cross-section samples of the AR and the SP samples after the cyclic oxidation at 850 °C. (Metal substrate on the left side)

Combined with the EDS-mapping results, the oxide phases of the scales on the cyclically exposed samples can be identified by X-ray diffraction as shown in Fig. 25. The inset of Fig. 25 differentiates the existing phases in the respective scales. The relative peak intensities indicate that the oxide scale on the SP sample is predominantly composed of Cr-rich oxides, such as $(Cr,Ti,Fe)_2O_3$ and $(Mn,Cr,Fe)_3O_4$, with some TiO_2, while the AR sample is predominantly composed of Fe_2O_3 with some $(Cr,Ti,Fe)_2O_3$, $NiFe_2O_4$, and $(Fe,Cr)_3O_4$.
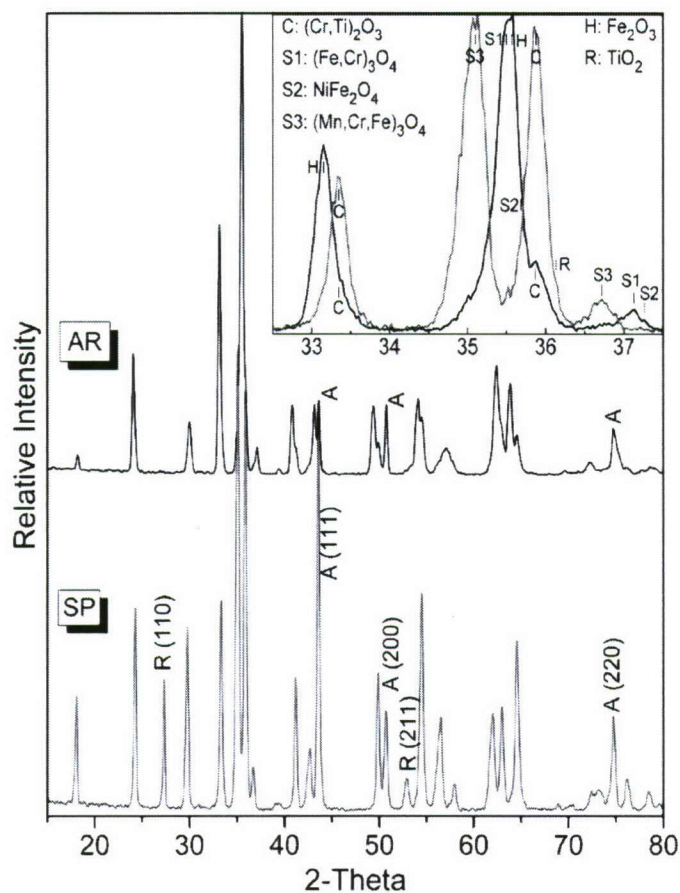
Fig. 25. X-ray diffraction patterns of the AR and the SP samples after cyclic oxidation at 850 °C. A, C, H, R, S1, S2, and S3 denote austenitic substrate, chorundum $(Cr,Ti)_2O_3$, hematite (Fe_2O_3), rutile (TiO_2), and spinels $(Fe,Cr)_3O_4$, $NiFe_2O_4$, and $(Mn,Cr,Fe)_3O_4$, respectively.

4.3. Discussion

The results of the SCW and cyclic oxidation tests indicate that the shot-peening processing on the alloy 800H resulted in different oxide microstructure compared to the AR samples. The results are summarized in Table 3. The thickness of the oxide scale on the SP samples was reduced to about half of that on the AR samples for both the SCW and cyclic oxidation tests. The microstructure of the oxide scale on the SP samples is simpler and dominated by Cr-rich oxides compared to that on the AR samples. The presence of Cr2O3 at the interface of the oxide scale and the metal on the SP samples is consistent with the observation of Matsuo et al., who studied steam oxidation tests of 18Cr-10Ni austenitic steels [69].

Table 3. Oxide microstructure of the AR and the SP samples exposed to the SCW at 500°C and the cyclic oxidation at 850°C. Species in bold denotes enrichment.

| Sample | Thickness (µm) | | Major Oxides (metal → surface) | |
	SCW	Cyclic	SCW	Cyclic Oxidation
AR	~3-4	~22	$(Ni,Cr)_3O_4$, $FeCr_2O_4$, Fe_3O_4, Fe_2O_3	$(Cr,Ti)_2O_3$, $NiFe_2O_4$, $FeCr_2O_4$, Fe_2O_3
SP	~1-2	~11	Cr_2O_3, $FeCr_2O_4$	$(Cr,Ti)_2O_3$, TiO_2, $(Mn,Cr,Fe)_3O_4$

The difference in the oxide microstructure mainly results from the grain size effect on the Cr flux since Cr has the highest diffusion coefficient in this system [70]. Based on the equations of the Cr flux via lattice and grain boundaries for a semi-infinite geometry assuming negligible transfer to and from the grain [71,72]:

(Equation 1) $\quad j_L \approx \dfrac{d^2 D_L (C_B - C_1)}{(\pi D_L t)^{1/2}}$

(Equation 2) $\quad j_B \approx \dfrac{2dw D_B (C_B - C_1)}{(\pi D_B t)^{1/2}}$

The flux ratio of Cr via grain boundaries versus lattice will be

(Equation 3) $\quad j_B / j_L = \dfrac{2w}{d} \left(\dfrac{D_B}{D_L} \right)^{1/2}$

where d is grain size, w is grain boundary width which is usually about 0.5 nm [73], D_L and D_B are the lattice and grain boundary diffusion coefficients, C_B and C_1 are the bulk concentration and fixed surface concentration, t is the period of oxidation. Since Incoloy alloy 800 has the same chemical composition as alloy 800H, the diffusion coefficients of Cr via lattice and grain boundaries in Incoloy alloy 800 are [74]:

$$D_{L,Cr} = 3.24 \times 10^{-4} \exp\left[-287.4 \text{kJ/mol}/(RT)\right] \text{m}^2/\text{s} \quad (T = 1060\text{-}1510 \text{ K})$$

$$D_{B,Cr} = 5.80 \times 10^{-5} \exp\left[-184.2 \text{kJ/mol}/(RT)\right] \text{m}^2/\text{s} \quad (T = 775\text{-}1170 \text{ K})$$

and should be applicable for alloy 800H. Thereby, the Cr flux ratio (j_B/j_L) as a function of grain size (d) can be calculated and is plotted in Fig. 26. The fraction of the Cr flux via grain boundaries [$j_B/(j_B+j_L)$] as a function of grain size (d) for alloy 800H is also plotted in Fig. 26. As the grain size decreases from ~100 μm for the AR samples to ~20 nm for the SP samples, the Cr flux ratio (j_B/j_L) increases from ~0.001 to ~5 and the fraction of Cr transported via grain boundaries increased from ~0.1% to ~80%. The significantly increased Cr flux via grain boundaries due to grain size refinement greatly promotes the formation of the predominant Cr-rich oxide on the SP samples.
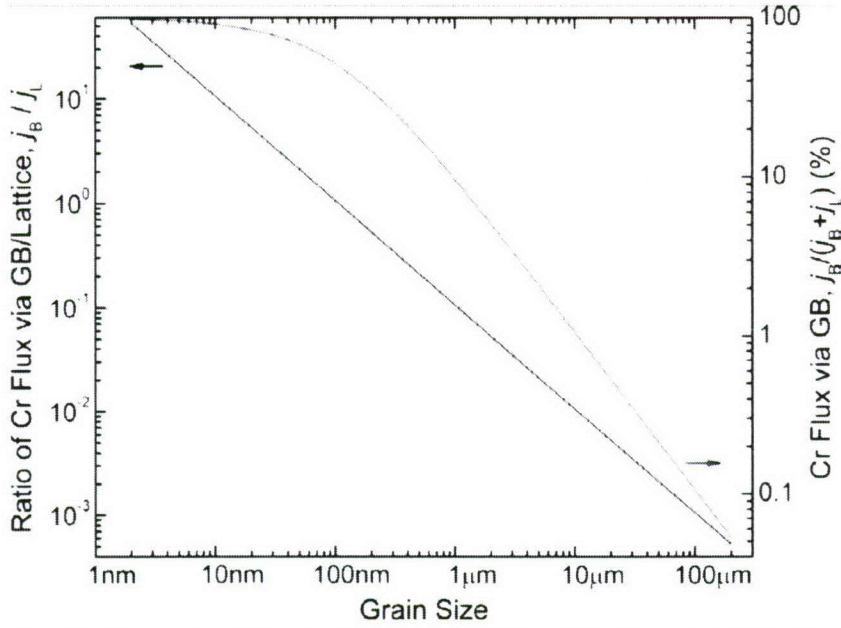
Fig. 26. Flux ratio of Cr via GB/Lattice (j_B/j_L) and Cr flux via GB [$j_B/(j_B+j_L)$] as a function of grain size.

The formation of Cr-rich oxides, such as Cr_2O_3 and $FeCr_2O_4$, improved not only the oxidation resistance but also the oxide exfoliation resistance because of the small difference in volume thermal expansion coefficients between the oxides and the metal. The volume thermal expansion coefficients of selected oxides and alloy 800H are plotted in Fig. 6. Thus, oxide exfoliation induced by thermal expansion mismatch had been mitigated by the shot-peening processing due to the absence of Fe_3O_4 (Table 3). The grain size of the oxide scale formed on the SP samples is much smaller than that on the AR samples, which is beneficial for mitigating the oxide exfoliation induced by thermal shock. This is because the thermal conductivity of the fine-grained surface layer decreases clearly if compared with that of the coarse-grained samples due to the larger volume fraction of the interfaces in the ultrafine-grained layer [75].

Although Cr oxide is protective generally, the Cr volatility of Cr-containing oxides becomes a problem at high temperatures. Cr volatility may have occurred during the cyclic oxidation testing, which resulted in extensive cracked bubbles on the AR samples. Fig. 27 shows the Cr vapor pressure of Cr_2O_3, $FeCr_2O_4$, and $LaCrO_3$ [76]. Compared to the Cr_2O_3, $FeCr_2O_4$ has a lower and $LaCrO_3$ has the lowest Cr vapor pressure. Although the data for the Cr vapor pressure of $(Cr,Ti)_2O_3$ is not available, it is expected to be similar to $LaCrO_3$ because both La and Ti are hexagonal structure instead of cubic structure like Fe. Therefore, the SP samples with the high concentration of Ti in $(Cr,Ti)_2O_3$ and the presence of TiO_2 mitigated the Cr volatilization compared to the AR samples. Additionally, the compressive stress induced by the shot-peening processing may have contributed to mitigate the Cr volatilization and oxide exfoliation on the SP samples.
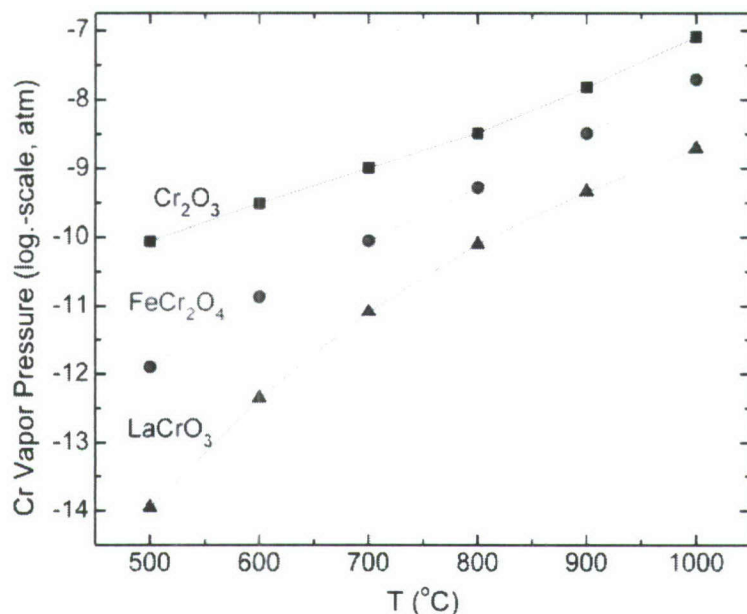
Fig. 27. Temperature dependence of Cr vapor pressures of Cr_2O_3, $FeCr_2O_4$, and $LaCrO_3$.

5. Effect of residual strains on corrosion

Weight loss was observed for the CVD-SiC samples exposed to the SCW at 500°C for ~1, ~2, and ~3 weeks and the weight loss increased with exposure time. Kim et al. reported that preferential corrosion of CVD-SiC in water at 360°C had occurred along GBs, revealing large columnar grains [77]. They suggested that the preferential GB corrosion was likely due to the higher energy of SiC at the grain boundaries relative to the SiC within the grains and that as the corrosion reaction proceeded, sufficient amounts of SiC were removed from the GBs resulting in the drop-out of grains into the water [7744]. The drop-out of grains into the water, as opposed to dissolution of hydrolyzed SiC, was identified as the source of the abrupt increase in weight loss after the 10-day exposure [77]. In the present study, the amount of weight loss of the 25 ppb oxygen exposed samples was much lower than that reported by Kim, et al. Moreover, the abrupt increase in weight loss reported by Kim, et al., after 10 days was not seen in the present study.

Fig. 28 shows SEM micrographs of cross sections of the AR CVD-SiC and the SCW-exposed sample for ~3 weeks. Large columnar grains that are typical of CVD 3C-SiC are evident. After the ~3-week exposure, rough surface is seen at a depth of 3-5 microns.
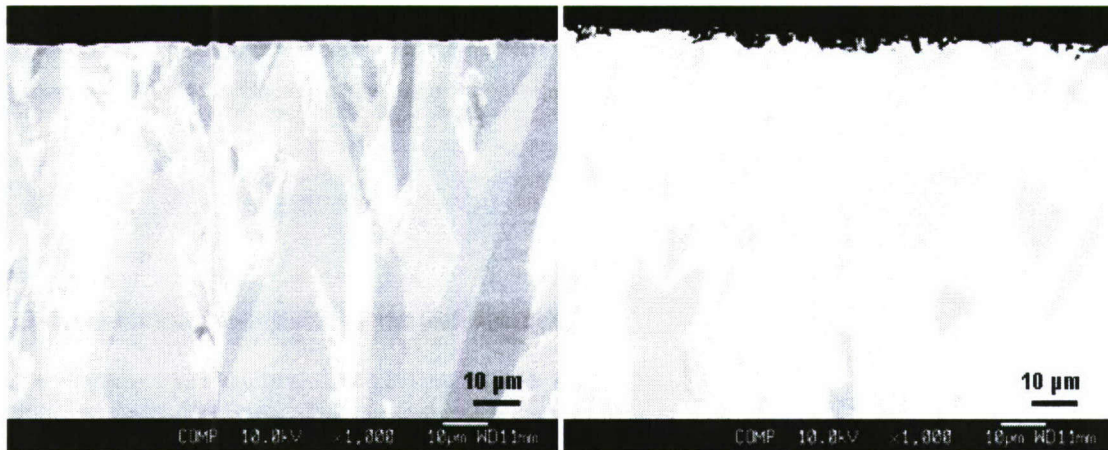
Fig. 28. SEM micrographs of polished cross sections of the AR CVD-SiC (left), and after 3-week exposure to the SCW at 500°C with 25 ppb O_2 (right).

Fig. 29 shows the surface morphologies of the AR CVD-SiC and after exposure to the SCW for ~1, ~2, and ~3 weeks. The surface features on the AR sample are the result of polishing artifacts. After exposure to the SCW, SiC grains can be distinguished on the surface and the amount of SiC removed clearly increases with exposure time. Corrosion attack occurred at both inside grains and GBs.
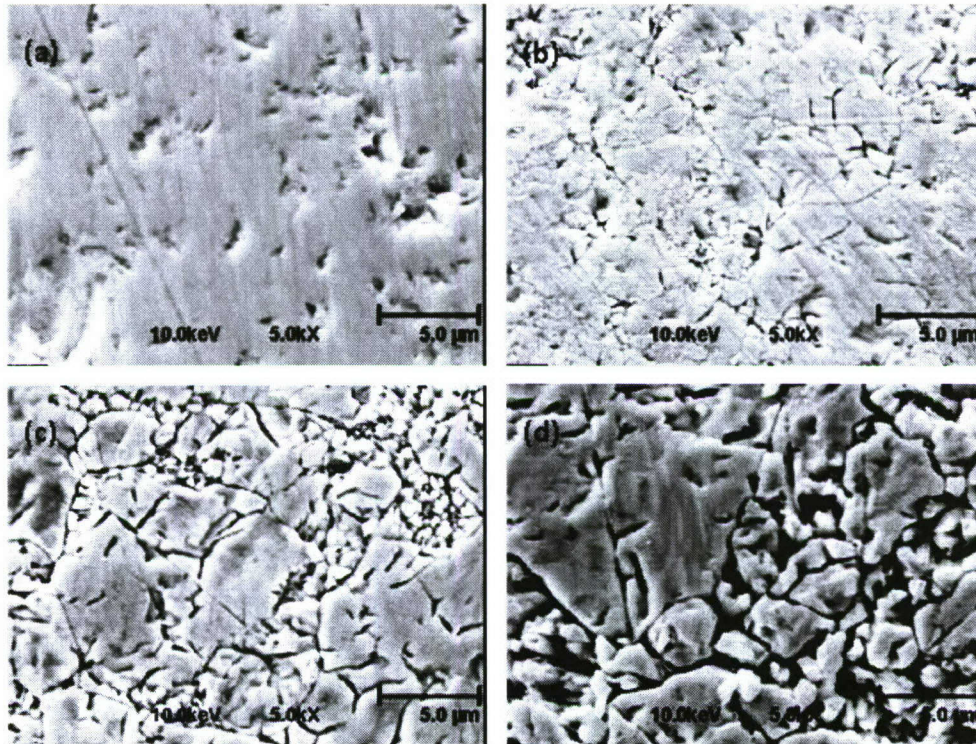

Fig. 29. SEM micrographs of surfaces for: (a) AR CVD-SiC; (b) after 1-week exposure; (c) after 2-week exposure; and (d) after 3-week exposure.

The microstructure of the AR CVD-SiC on the plan-view and cross-section directions is shown in **Fig. 30**. The plan-view sample is composed of equiaxial grains, while the cross-section sample is composed of columnar grains. The inverse pole figures (IPF) indicate that large grains are predominantly occupied by a near (111) texture aligned with the deposition direction of the CVD-SiC. The strain distribution is represented by local average misorientation between each EBSD data point measurement and its neighbors excluding any higher angle boundaries (>5°). The strains congregated at small grains surrounding large grains, which may have resulted from the constraint growth of the small grains by the large grains prevalent with a near (111) texture along the deposition direction during CVD. The area fraction of strains on the plan-view sample is greater than that on the cross-section sample.
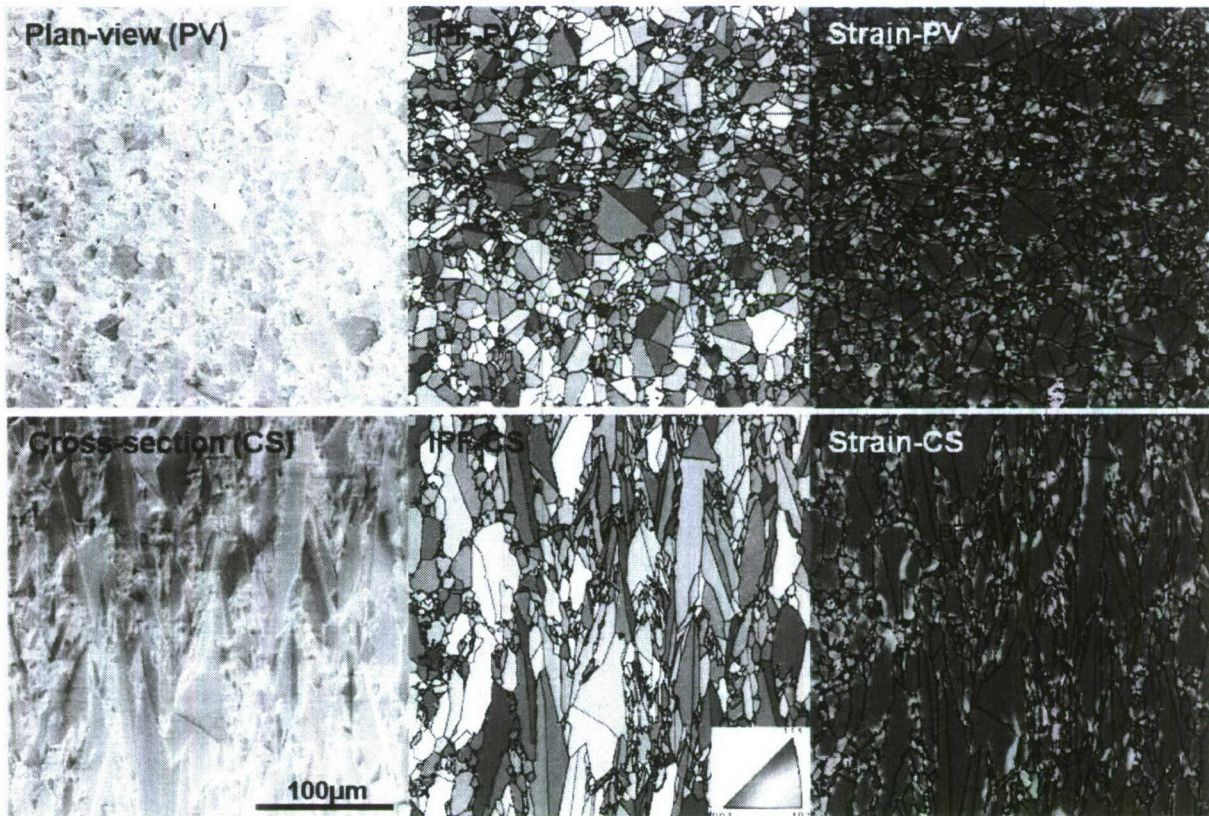
Fig. 30. Plan-view (PV) and cross-section (CS) microstructure of the AR CVD-SiC: secondary electron images (SEIs, left column) and EBSD maps coded with inverse pole figure (IPF, center column) and strain distribution (▦ 0° – 5° average misorientation).

The microstructure of the plan-view and cross-section samples exposed to the SCW at 500°C with 25 ppb for ~2 weeks is shown in **Fig. 31**. The secondary electron image associated with the EBSD maps (IPF, GBs, and strains) of the plan-view sample indicate that corrosion attack preferentially occurred at regions with a high density of strain. Σ3 boundaries, which generally do not associate with strains, were not attacked by corrosion. Similar results were observed on

the cross-section sample. However, the amount of corrosion attack on the cross-section sample is less than that on the plan-view sample, which may be due to the smaller fraction of strain area on the cross-section sample.
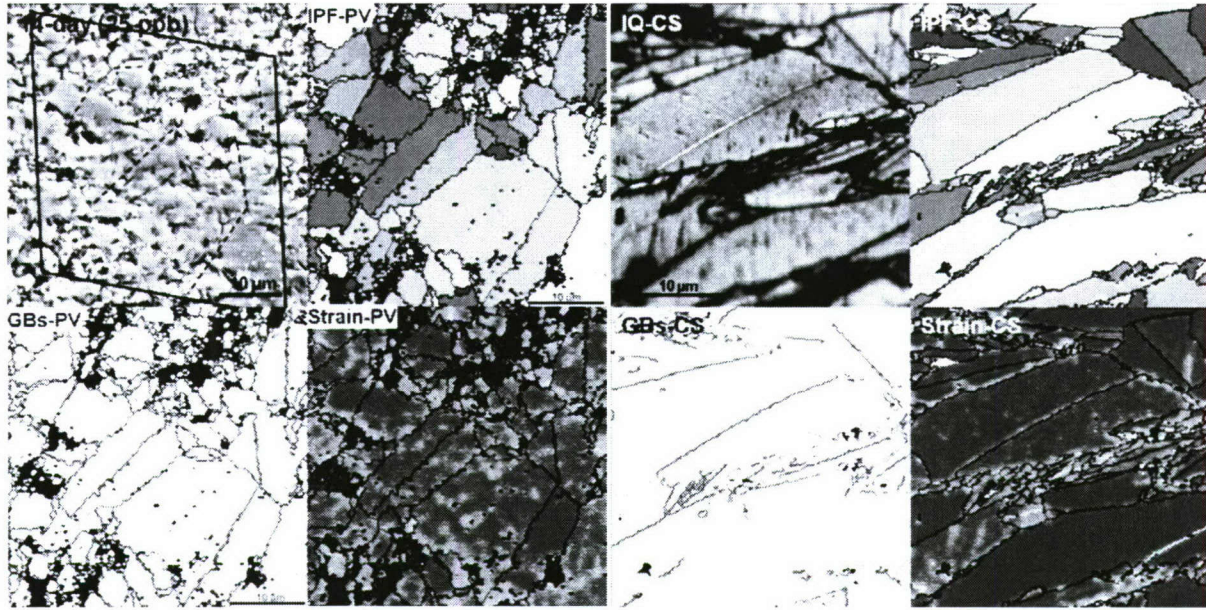

Fig. 31. Plan-view (PV) and cross-section (CS) of 2-week SCW-exposed CVD SiC, where IQ, IPF, GBs, and Strain correspond to EBSD maps of image quality, inverse pole figure, grain boundaries, and strain distribution (▭ $0°$ − $5°$ average misorientation), respectively. Grain boundaries (GBs) are highlighted with blue and red/green denoting $\Sigma3$ boundaries and $\Sigma5$- $\Sigma29$ boundaries, respectively. The black regions on the EBSD maps denote unidentified regions due to high density of defects.

The micro-texture of the grains on the plan-view and cross-section samples prior to and after the SCW exposure testing was analyzed using IPFs based on the EBSD analyses of the two samples on an area of 100×160 μm^2. The results are shown in **Fig. 32**. Both the plan-view and the cross-section samples prior to the SCW exposure exhibit a strong (113) texture aligned with the deposition direction (the plan-view surface normal). In addition to the (113) texture, a near (335) texture with an intensity similar to the (113) texture is presented on the cross-section sample. In contrast, slightly dispersive textures spread around (111) on the plan-view sample. After the SCW testing, the (113) texture tends to be intensified for both the plan-view and the cross-section samples. Additionally, the textures are changed to be close to (111). A mild (111) texture was formed on the cross-section sample with the decrease of the near (335) texture.
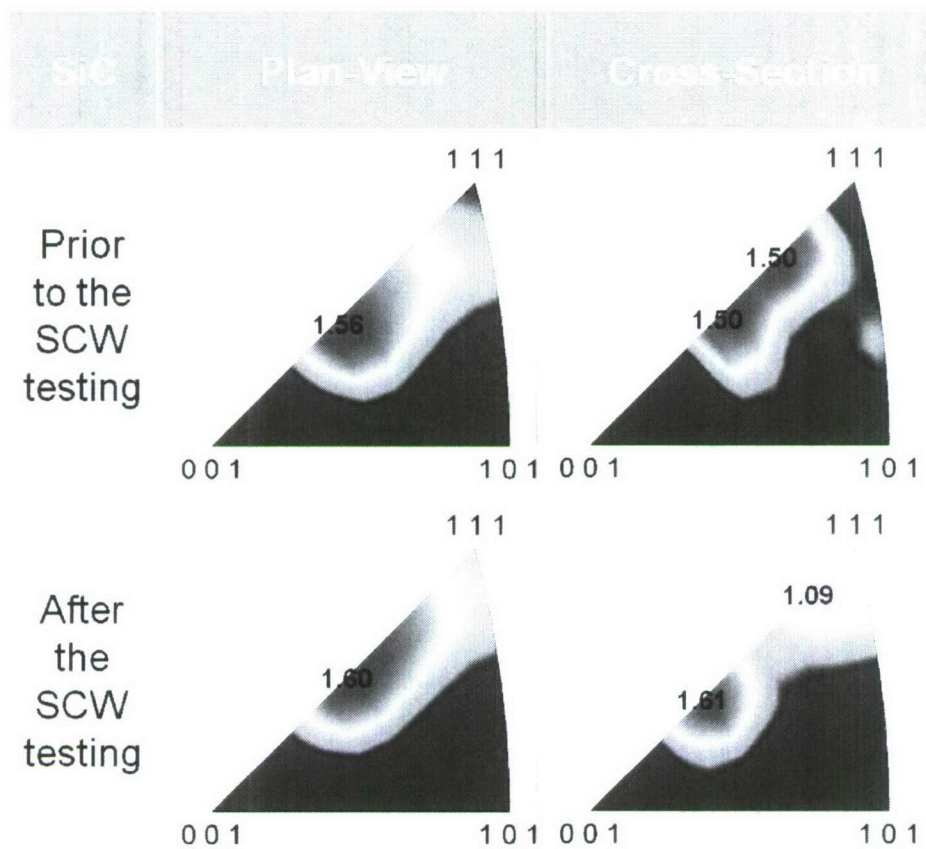
Fig. 32. IPFs of the plan-view and cross-section SiC samples prior to and after the SCW testing for 2-week indicating the textures aligned with the deposition direction of the CVD-SiC.

The surface roughness of the samples prior to and after the SCW exposure for 2-weeks was analyzed using a Zygo NewView 3D optical profile. The results are listed in **Table 4**. Both the plan-view and the cross-section samples became rougher after the SCW exposure. However, the roughness on the plan-view sample after the SCW exposure is greater than that on the cross-section sample. The root-mean-square roughness on the cross-section sample after the SCW exposure is ~60% of that on the plan-view sample. Although the peak-to-valley height on the cross-section sample was slightly larger than that on the plan-view sample, it became smaller on the cross-section sample after the SCW exposure.

Table 4. Root-mean-square (rms) and peak-to-valley (PV) roughness of the CVD-SiC prior to and after the SCW testing at 500°C with 25 ppb dissolved oxygen for 2-week. (Roughness was averaged from 5 data)

Orientation	Plan-view	Cross-section	Plan-view	Cross-section
rms (μm)	0.037±0.009	0.055±0.011	0.309±0.015	0.189±0.013
PV (μm)	0.505±0.025	0.572±0.021	9.570±0.916	9.157±0.898

6. Summary

Grain boundaries (Grain boundary engineering)

GBE was applied to the alloys 800H and 617 by means of TMP to improve protective oxidation behavior. The GBCD of the GBE-treated samples had been optimized to possess a greatly increased fraction of low-Σ CSLBs and decreased fraction of general boundaries. The optimized GBCD is sustainable at temperatures up to 760°C and 1000°C for alloys 800H and 617, respectively. The SCW testing results indicate that the GBE-treatment on the alloy 800H greatly mitigated oxide exfoliation which extensively occurred on the AR samples. Oxide scales in a layer structure formed on both the AR and the GBE-treated samples with the outer layer composed of hematite and magnetite, and the inner layer composed of a mixture of austenite (substrate) and spinel at 500°C. The oxide scale on the AR samples has a sharper strain change and anisotropic strong texture compared to that on the GBE-treated samples, which led to the oxide exfoliation that occurred on the AR samples. The protective oxidation behavior of GBE-treated samples represented by the improved exfoliation resistance and slower oxidation rate (thinner inner layer) is believed to be attributed to the highly increased population of low-Σ CSLBs. The GBE-treatment reduced the oxidation rate (weight grain) to ~1/2 of the AR samples of the alloy 617 as evaluated by the cyclic oxidation tests in air at 1000°C. The SCW exposure results indicate the GBE-treatment resulted in a more compact oxide scale with a continuous chromium oxide surface layer compared to the AR samples of the alloy 617.

The TMP did not significantly improve the oxidation resistance of the ferritic-martensitic steel HCM12A. A dual-layer structure (outer magnetite and inner spinel) oxide scale without exfoliation formed on both the AR and the TMP samples of the HCM12A. The outer magnetite layer being composed of a large fraction of small equiaxial grains was formed on the TMP samples compared to the large fraction of large columnar grains in the magnetite layer on the AR samples. The (101) texture in the AR samples had been changed to a near (101) texture in the TMP samples, which may have contributed to reduce the formation of columnar magnetite grains on the TMP samples.

Grain size (Shot-peening)

The effect of shot-peening (SP) on the oxidation behavior was studied using supercritical water (SCW) and cyclic oxidation tests. It was found that an ~70 μm deformation zone depth was produced by the SP processing on the alloy 800H. The deformation zone is composed of two microstructural regions: an ultrafine-grained region at surface and a sequential transition region at the subsurface. The thickness of the oxide scale formed on the SP samples is about half of that on the as-received (AR) samples for the SCW and cyclic oxidation tests. The oxide scale on the SP samples is simpler and dominated by Cr-rich oxides, such as Cr_2O_3 and $FeCr_2O_4$, as compared to the AR samples. The ultrafine grains induced by the SP increased the population of grain boundaries resulting in an increased Cr diffusivity to assist in the formation of Cr and Cr-rich oxides. Oxide exfoliation induced by thermal expansion mismatch was greatly mitigated by preventing the formation of magnetite (Fe_3O_4) on the SP samples. The Cr volatilization of the chromium oxide was reduced on the SP samples during the cyclic oxidation tests, which may have resulted from the formation of Ti-rich chromium oxide such as $(Cr,Ti)_2O_3$ instead of Cr_2O_3.

Residual strains

The microstructure analysis of the CVD-SiC indicates that the material is composed of two types of grains. Clusters of small grains are isolated among large columnar (cross-sectional view) or equiaxial (plan-view) grains. A high level of residual strains exists at the clusters of small grains. The localized strains may have developed in the SiC when cooled down from the deposition temperature as a result of the defects and local anisotropies in the material. Most of the dissolution/corrosion was observed at the zones with a high level of residual strains. The cross-section samples had less corrosion attack than the plan-view samples because of the smaller fraction of residual strains on the cross-section samples. Moreover, the small grains would lead to higher grain boundary area in these zones, and a greater tendency to lose grains via erosion once sufficient corrosion of the grain boundaries had occurred. The types of grain boundaries did not show significant effect on the corrosion. For example, the general grain boundaries did not show severe corrosion compared to $\Sigma 3$ boundaries for the large grains.

List of Publications

1) L. Tan, K. Sridharan, T.R. Allen, R.K. Nanstad, D.A. McClintock, Microstructure tailoring for property improvements by grain boundary engineering, Journal of Nuclear Materials 374 (2008) 270-280.

2) L. Tan, X. Ren, K. Sridharan, T.R. Allen, Effect of shot-peening on the oxidation of alloy 800H exposed to supercritical water and cyclic oxidation, Corrosion Science, doi:10.1016/j.corsci.2008.04.008.

3) L. Tan, K. Sridharan, T.R. Allen, Altering corrosion response via grain boundary engineering, Materials Science Forum 2008.

4) L. Tan, X. Ren, K. Sridharan, T.R. Allen, Corrosion behavior of Ni-base alloys for advanced high temperature water-cooled nuclear plants, Corrosion Science, submitted.

References

[1] P.E.J. Flewitt, R.K. Wild, Grain Boundaries – Their Microstructure and Chemistry, John Wiley & Sons Ltd, England, 2001.

[2] V. Randle, The Role of the Coincidence Site Lattice in Grain Boundary Engineering, The Institute of Materials, London, 1996.

[3] Y. Pan, B.L. Adams, T. Olson, N. Panayotou, Grain-boundary structure effects on intergranular stress corrosion cracking of alloy X-750, Acta Mater. 44 (1996) 4685-4695.

[4] V.Y. Gertsman, S.M. Bruemmer, Study of grain boundary character along intergranular stress corrosion crack paths in austenitic alloys, Acta Mater. 49 (2001) 1589-1598.

[5] S. Yamaura, Y. Igarashi, S. Tsurekawa, T. Watanabe, Grain boundary engineering for the control of oxidation embrittlement. In: A. Meike (Eds.), Properties of Complex Inorganic Solids 2, (Proceedings of the International Alloy Conference), 2nd, Davos, Switzerland, Aug. 8-13, 1999. Kluwer Academic/Plenum Publishers, New York, NY, 2000, p. 27-37.

[6] U. Erb, P. Lin, S. Kim, K.T. Aust, F. Gonzalez, G. Palumbo, Grain boundary engineering in nanocrystalline and polycrystalline materials, in: T.S. Srivatsan, R.A. Varin (Eds.), Proceedings of the 10th International Symposium on Processing and Fabrication of Advanced Materials, Indianapolis, IN, USA, 5-8 November, 2001, p. 3.

[7] E.M. Lehockey, G. Palumbo, P. Lin, Improving the weldability of service performance of nickel- and iron-based superalloys by grain boundary engineering, Metall. Mater. Trans. A 29 (1998) 3069-3080.

[8] D.S. Lee, H.S. Ryoo, S.K. Hwang, A grain boundary engineering approach to promote special boundaries in Pb-base alloy, Mat. Sci. Eng. A 354 (2003) 106-111.

[9] M. Shimada, H. Kokawa, Z.J. Wang, Y.S. Sato, I. Karibe, Optimization of grain boundary character distribution for intergranular corrosion resistant 304 stainless steel by twin-induced grain boundary engineering, Acta Mater. 50 (2002) 2331-2341.

[10] R.K. Singh Raman, J.B. Gnanamoorthy, S.K. Roy. Influence of alloy grain size on the high temperature oxidation behavior of some steels with different Cr contents. *Trans. Indian Inst. Met.* 45 (1992) 391-398.

[11] X. Peng, J. Yan, Y. Zhou, F. Wang. Effect of grain refinement on the resistance of 304 stainless steel to breakaway oxidation in wet air. *Acta Mater.* 53 (2005) 5079-5088.

[12] V. Rollins, T. Pyle, Strain enhanced dissolution effects in the corrosion-fatigue failure of metals, Nature 254 (1975) 322-323.

[13] A.I. Rusanov, N.B. Ur'ev, P.V. Eryukin, T.G. Movchan, N.E. Esipova, Discovery of the effect of the stain sign in stress corrosion phenomena, Doklady Physical Chemistry 395 (2004) 88-89.

[14] INCOLOY alloy 800H & 800HT, Technical Bulletin, Special Metals Publication SMC-047, March 2004. (http://www.specialmetals.com)

[15] Next generation nuclear plant materials research and development program plan, Idaho National Engineering and Environmental Laboratory, Bechtel BWXT Idaho, LLC, Sept. 2004, INEEL/EXT-04-02347.

[16] A Technology Roadmap for Generation IV Nuclear Energy Systems, US DOE Nuclear Energy Research Advisory Committee and the Generation IV International Forum, December 2002 (http://gif.inel.gov/roadmap).

[17] N. Otsuka, H. Fujikawa, Scaling of austenitic stainless steels and nickel-base alloys in high-temperature steam at 973 K, Corrosion 47 (1991) 240-248.

[18] F.A. Khalid, N. Hussain, K.A. Shahid, Microstructure and morphology of high temperature oxidation in superalloys, Mater Sci Eng A 265 (1999) 87-94.

[19] G.S. Was, T.R. Allen, Time, temperature, and dissolved oxygen dependence of oxidation of austenitic and ferritic-martensitic alloys in supercritical water, In: Proceedings of ICAPP '05, May 15-19, 2005, Seoul, Korea.

[20] "The spalling of steam-grown oxide from superheater and reheater tube steels," EPRI FP-686, Technical Planning Study 76-655, February 1978, Palo Alto, CA, USA.

[21] Next generation nuclear plant materials research and development program plan, Idaho National Engineering and Environmental Laboratory, Bechtel BWXT Idaho, LLC, Sept. 2004, INEEL/EXT-04-02347.

[22] F. Abe, H. Yoshida, Corrosion behaviours of heat resisting alloys in steam at 800 °C and 400 atm pressure, Z. Metallkde. 76 (1985) 219-225.

[23] G.R. Holcomb, S.D. Cramer, Jr. B.S. Covino, S.J. Bullard, M. Ziomek-Moroz, Ultra supercritical steamside oxidation, Report # DOE/ARC-05-003 (http://www.osti.gov/bridge/servlets/purl/859328-sO62ee/859328.PDF).

[24] P. Billot, D. Barbier, 2nd International Topical Meeting on High Temperature Reactor Technology, Beijing, China, Sept. 22-24, paper #A01.

[25] L. Tan, K. Sridharan, T.R. Allen, The effect of grain boundary engineering on the oxidation behavior of INCOLOY alloy 800H in supercritical water, J. Nucl. Mater. 348 (2006) 263-271.

[26] R.L. Klueh, D.R. Harries, Development of high (7-12%) chromium martensitic steels. In: High-Chromium Ferritic and Martensitic Steels for Nuclear Applications, 2001, ASTM International.

[27] F. Masuyama, New developments in steels for power generation boilers. In: R. Viswanathan, J. Nutting (Eds.), Advanced Heat Resistant Steels for Power Generation, Conference Proceedings, April 27-29, 1998, San Sebastian, Spain.

[28] R. Viswanathan, W.T. Bakker, Materials for Boilers in Ultra Supercritical Power Plants, In: Proceedings of 2000 International Joint Power Generation Conference (IJPGC2000-15049), Miami Beach, Florida, July 23-26, 2000.

[29] Z. Klenowicz, K. Darowicki, Corrosion Reviews, 19 (2001) 467.

[30] S.N. Rosenwasser et al., J. Nucl. Mater., 85 & 86 (1979) 177.

31 D.R. Harries, in: Proceedings of Topical Conference on Ferritic Steels for Use in Nuclear Energy Technologies, Eds. J.W. Davis and D.J. Michel (The Metallurgical Society of AIME, Warrendale, PA, 1984) 141.

32 A. Fry, S. Osgerby, M. Wright, Oxidation of Alloys in Steam Environments – A Review, National Physical Laboratory (NPL) Report MATC(A)90, Sept. 2002. ISSN: 1473-2734.

33 P.J. Ennis, Y. Wouters, J. Quadakkers, The Effects of Oxidation on the Service Life of 9-12% Chromium Steels, In: Advanced Heat Resistant Steel for Power Generation, Institute of Materials, 1999, pp. 457.

34 K. Nakagawa, I. Kajigaya, T. Yanagisawa, M. Sato, M. Abe, Study of Corrosion Resistance of Newly Developed 9-12%Cr Steels for Advanced Units, In: Advanced Heat Resistance Steel for Power Generation, Institute of Materials, 1999, pp. 468.

35 Y. Sawaragi, K. Miyata, S. Yamamoto, F. Masuyama, N. Komai, T. Yokoyama, Properties after service exposure of 2.25Cr-1.6W-V,Nb (HCM2S) and 12Cr-0.4Mo-2W-1Cu-V,Nb (HCM12A) steel tubes in a power boiler. In: R. Viswanathan, J. Nutting (Eds.), Advanced Heat Resistant Steels for Power Generation, Conference Proceedings, San Sebastian, Spain, 27-29 April, 1998.

36 K.A. Burrill, Water Chemistries and Corrosion Product Transport in Supercritical Water in Reactor Heat Transport Systems, Water Chemistry of Nuclear Reactor Systems 8, Proceedings of the conference organized by the British Nuclear Energy Society and held in Bournemouth, UK, Oct. 22-26, 2000, pp. 357-363.

37 E.E. Bloom, "The Challenge of Developing Structural Materials for Fusion Power Systems, "Journal of Nuclear Materials 263: 7-17 Part A, Oct 1998.

38 D. J. Senor, G. E. Youngblood, C. E. Moore, D. J. Trimble, G. A. Newsome, and J. J. Woods, "Effects of Neutron Irradiation on Thermal Conductivity of SiC-based Composites and Monolithic Ceramics," Fusion Technology, 30 (3): 943-955 Part 2A, DEC 1996.

39 H. Hirayama, T. Kawakubo, A. Goto, and T. Kaneko, "Corrosion Behavior of Silicon Carbide in 290°C Water," J. Amer. Ceram. Soc., 72 [11], 2049-2053 (1989).

40 N. S. Jacobson, Y. G. Gogotsi, and M. Yoshimura, "Thermodynamic and Experimental Study of Carbon Formation on Carbides under Hydrothermal Conditions," J. Mater. Chem., 5, 595-601 (1995).

41 Y. Gogotsi, K. Nickel, D. Bahloul-Hourlier, T. Merie-Mejean, G. Khomenko and K. Skjerlie, "Structure of Carbon Produced by Hydrothermal Treatment of β -SiC Powder," J. Mater. Chem., 6[4], 595-604 (1996).

42 T. Kraft, K. G. Nickel, and Y. G. Gogotsi, "Hydrothermal Degradation of Chemical Vapor Deposited SiC Fibres," J. Mater. Sci., 33, 4357-4363 (1998).

43 W. Kim, H. Hwang, and J. Park, "Corrosion Behavior of Reaction-Bonded Silicon Carbide Ceramics in High-Temperature Water," J. Mater. Sci. Letters, 21, 733-735 (2002).

44 W. Kim, H. Hwang, J. Park, and W. Ryu, "Corrosion Behavior of Sintered and Chemically Vapor Deposited Silicon Carbide Ceramics in Water at 360°C," J. Mater. Sci. Letters, 22, 581-584 (2003).

45 L. Tan, T.R. Allen, An EBSD study of grain boundary engineered INCOLOY alloy 800H, Metallurgical and Materials Transactions A 36(7) (2005) 1921-1925.

46 L. Tan, K. Sridharan, T.R. Allen, Effect of thermomechanical processing on grain boundary character distribution of a Ni-based superalloy, J. Nucl. Mater. 371 (2007) 171-175.

[47] F. Abe, H. Araki, H. Yoshida, M. Okada, R. Watanabe, The effect of grain-size on the corrosion behavior of Inconel 600 in high-temperature steam, Corros. Sci. 21 (1981) 819.

[48] K. Sridharan, A. Zillmer, J.R. Licht, T.R. Allen, M.H. Anderson, L. Tan, Corrosion behavior of candidate alloys for supercritical water reactors, Proceedings of ICAPP 04, Pittsburgh, PA, 2004, p. 537.

[49] D.P. Field, Ultramicroscopy 67 (1997) 1.

[50] M. Shimada, H. Kokawa, Z.J. Wang, Y.S. Sato, I. Karibe. Optimization of grain boundary character distribution for intergranular corrosion resistance 304 stainless steel by twin-induced grain boundary engineering. *Acta Mater.* 50 (2002) 2331-2341.

[51] V.Y. Gertsman, S.M. Bruemmer. Study of grain boundary character along intergranular stress corrosion crack paths in austenitic alloys. *Acta Mater.* 49 (2001) 1589-1598.

[52] G. Palumbo, K.T. Aust, U. Erb, P.J. King, A.M. Brennenstuhl, P.C. Lichtenberger, Phys. Status Solidi A, 131 (1992) 425-428.

[53] V.Y. Gertsman, S.M. Bruemmer, Study of grain boundary character along intergranular stress corrosion crack paths in austenitic alloys, Acta Mater. 49 (2001) 1589-1598.

[54] R.M. Cornell, U. Schwertmann, The Iron Oxides – Structure, Properties, Reactions, Occurences and Uses, second ed., Wiley-VCH Verlag GmbH & Co. KGaA, Germany, 2003.

[55] B.J. Skinner, Thermal expansion, in: S.P. Clark, Jr. (Ed.), Handbook of Physical Constants, Geol. Soc. Am. Mem., 1966, pp. 75-95.

[56] Y. Fei, Thermal expansion, in: Mineral Physics and Crystallography – A Handbook of Physical Constants, the American Geophysical Union Reference Shelf 2, 1995.

[57] C. Haavik, S. Stølen, H. Fjellvåg, M. Hanfland, D. Häusermann, Equation of state of magnetite and its high-pressure modification: thermodynamics of the Fe-O system at high pressure, American Mineralogist 85 (2000) 514-523.

[58] H.J. Reichmann, S.D. Jacobsen, Sound velocities and elastic constants of ZnAl2O4 spinel and implications for spinel-elasticity systematic, American Mineralogist, 91 (2006) 1049-1054.

[59] A.L. Edwards, For Computer Heat-Conduction Calculations A Compilation of Thermal Properties Data, UCRL-50589, Feb. 24, 1969.

[60] N.M. Hwang, B.J. Lee, C.H. Han. Texture evolution by grain growth under a system of anisotropic grain boundary energy. *Scripta Mater.* 37 (1997) 1761-1767.

[61] N. Ma, A. Kazaryan, S.A. Dregia, Y. Wang. Computer simulation of texture evolution during grain growth: effect of boundary properties and initial microstructure. *Acta Mater.* 52 (2004) 3869-3879.

[62] H. Sankur, W.J. Gunning, J.F. DeNatale. Intrinsic stress and structural-properties of mixed composition thin-films. *Appl. Optics* 27 (1988) 1564-1567.

[63] T. Watanabe, S. Tsurekawa, The control of brittleness and development of desirable mechanical properties in polycrystalline systems by grain boundary engineering, Acta Mater. 47 (1999) 4171-4185.

[64] C.E. Campbell, W.J. Boettinger, U.R. Kattner, Development of a diffusion mobility database for Ni-base superalloys, Acta Mater. 50 (2002) 775-792.

[65] S.J. Rothman, L.J. Nowicki, G.E. Murch, Self-diffusion in austenitic Fe-Cr-Ni alloys, J. Phys. F: Metal Phys. 10 (1980) 383-398.

[66] G.K. Williamson, W.H. Hall, X-ray line broadening from filed aluminum and tungsten, Acta Metal. 1 (1953) 22-31.

[67] X. Wang, J. Wang, L. Xiong, G. Liu, Defect characteristics in the surface nanocrystallined material treated by high-energy shot peening, Mater. Sci. For. 445-446 (2004) 210-212.

[68] N. Hussain, K.A. Shahid, I.H. Khan, S. Rahman, Oxidation of high-temperature alloys (supaeralloys) at elevated temperatures in air: I, Oxid. Metal. 41 (1994) 251-269.

[69] H. Matsuo, Y. Nishiyama, Y. Yamadera, Steam oxidation properties of fine-grain steels, in: Proceedings from the Fourth International Conference on Advances in Materials Technology of Fossil Power Plants, Hilton Head Island, South Carolina, Oct. 25-28, 2004.

[70] S.J. Rothman, L.J. Nowicki, G.E. Murch, Self-diffusion in austenitic Fe-Cr-Ni alloys, J. Phys. F: Metal Phys. 10 (1980) 383-398.

[71] R.C. Lobb, H.E. Evans, Formation of protective oxide film on chromium-depleted stainless steel, Metal Sci. June (1981) 267-274.

[72] J. Crank, The Mathematics of Diffusion, 2nd Ed., Oxford University Press, 1975, p. 32.

[73] J.C. Fisher, Calculation of diffusion penetration curves for surface and grain boundary diffusion, J. Appl. Phys. 22 (1951) 74-82.

[74] A.R. Paul, K.N.G. Kaimal, M.C. Naik, S.R. Dharwadkar, Lattice and grain boundary diffusion of chromium in superalloy Incoloy-800, J. Nucl. Mater. 217 (1994) 75-81.

[75] F.A. Guo, N. Trannoy, J. Lu, Characterization of the thermal properties by scanning thermal microscopy in ultrafine-grained iron surface layer produced by ultrasonic shot peening, Mater. Chem. Phys. 96 (2006) 59-65.

[76] Z. Yang, G. Maupin, S. Simner, P. Singh, J. Stevenson, G. Xia, Advanced interconnect development, in: SECA Annual Workshop and Core Technology Program Peer Review, Tampa, FL, Jan. 28, 2005.

[77] W. Kim, H. Hwang, J. Park, and W. Ryu, "Corrosion Behavior of Sintered and Chemically Vapor Deposited Silicon Carbide Ceramics in Water at 360°C," J. Mater. Sci. Letters, 22, 581-584 (2003).